Applied Materials Today 50 (2026) 103248

Contents lists available at ScienceDirect

Applied Materials Today

journal homepage: www.elsevier.com/locate/apmt

Functional vanadium oxide nanostructures fabricated via atomic layer deposition: A review

Carina Hedrich [a], Robert H. Blick [b], Martin Ritter [a], Robert Zierold [b], Kaline P. Furlan [c,*]

[a] Hamburg University of Technology (TUHH), Electron Microscopy Unit (BeEM), Eißendorfer Straße 42, Hamburg 21073, Germany
[b] University of Hamburg, Center for Hybrid Nanostructures (CHyN), Luruper Chaussee 149, Hamburg 22761, Germany
[c] Karlsruhe Institute of Technology (KIT), Institute of for Applied Materials (IAM), Ceramic Materials and Technologies (KWT), Haid-und-Neu-Str. 7, Karlsruhe 76131, Germany

ARTICLE INFO

Keywords:
Vanadium oxide
Nanostructures
Atomic layer deposition
Thermal annealing
Phase control
Functional oxides

ABSTRACT

Vanadium oxide nanostructures have emerged as a promising material system for a wide range of applications based on their structural, electronic, optical, and catalytic properties. The multiple phases of vanadium oxides, e.g., V_2O_3, VO_2, and V_2O_5, feature distinct crystal structures and properties which contribute to their versatility. There are several methods to fabricate vanadium oxide nanostructures such as sol-gel synthesis, hydrothermal methods, physical vapor deposition, sputter deposition, chemical vapor deposition, atomic layer deposition (ALD), and solid-state reactions. From those techniques, ALD offers precise control over the conformality, thickness, and composition of thin films leading to unique possibilities for the functionalization of previously prepared nanostructured templates with vanadium oxides. This review summarizes recent advancements in the synthesis of ALD-based vanadium oxide nanostructures focusing on suitable ALD precursors, ALD process conditions, and required post-deposition thermal annealing treatments to transform the as-deposited vanadium oxide films to distinguished crystalline phases. The functional properties of ALD-based vanadium oxide nanostructures in catalysis, electrochemical energy storage, sensors, and stimuli-responsive "smart" devices are presented. Moreover, existing challenges in fabrication and practical application are discussed. Finally, future perspectives on tailoring the properties of ALD-based vanadium oxide nanostructures by adjusting templates, optimizing the vanadium oxide film thickness, or utilizing supercycle ALD processes are outlined, which can pave the way for sustainable applications and "smart" devices.

1. Introduction

Vanadium oxides exist in a plethora of stoichiometries and crystalline phases which determine a multitude of different functional properties [1–5]. These include catalytic activity, electrochemical energy storage capability, gas sensing properties, and insulator-to-metal transition (IMT) related properties [1–7]. Such vanadium oxide (V_xO_y) structures can be synthesized by several methods, for instance hydrothermal method [1,3,4], sol-gel technique [1,4], chemical vapor deposition (CVD) [1,2], physical vapor deposition (PVD) [1,8], sputter deposition [1,7,9], solid-state reactions [5], and atomic layer deposition (ALD) [2,7]. Among the V_xO_y structures produced by these methods, nanostructured V_xO_y – in which at least one dimension is in the nanometer regime – provides improved properties and/or great potential for new functionalities when in comparison to bulk materials, due to their high surface-to-volume ratio and confinement effects [1,3–6,8]. Besides directly synthesizing V_xO_y nanostructures, they can also be fabricated by first creating a nanostructured substrate of a different material and subsequently functionalizing this substrate with V_xO_y. Such a two-step approach allows for larger design freedom since the nanostructured template shaping process is independent from the V_xO_y functionalization. Hence, in the first step, the template could be shaped in many different formats and even prepared under conditions that are not suitable for the formation of V_xO_y. Moreover, the template material can be freely chosen which can add further functionalities such as conductivity to the template. In the second step, the nanostructured template is functionalized with V_xO_y for example by wet impregnation, CVD, sputter deposition, PVD, or ALD.

From these functionalization techniques, ALD is particularly interesting because it offers the possibility of conformally coating even

* Corresponding author.
E-mail address: kaline.furlan@kit.edu (K.P. Furlan).

https://doi.org/10.1016/j.apmt.2026.103248
Received 22 February 2026; Received in revised form 13 April 2026; Accepted 22 April 2026
Available online 5 May 2026

complex shaped substrates due to its inherent self-limiting gas-solid surface reactions [10–13] and precise control of the growth rate – denoted as growth per cycle (GPC) – often in the sub-nanometer range [10–12]. A standard ALD process is divided into sequential half-cycles consisting of individual pulses and exposures of a single precursor separated by pumping of the excess unreacted precursors [10–17]. Thermal ALD is the most commonly used type, where the temperature of the ALD reactor activates the chemical reaction between the precursor molecules and the substrate [10]. In plasma-enhanced ALD (PEALD), one precursor is substituted by a gas plasma to generate reactive species allowing for a lower required system temperature which enables ALD of materials that cannot be deposited by thermal ALD processes [10,14].

In general, ALD processes can be used to deposit a plethora of materials including oxides, nitrides, fluorides, sulfides, selenides, tellurides, and metals [11,14]. Furthermore, the same material can be deposited by using different precursors, where their functional groups determine the possible reactions and the precursors' reactivity. To deposit compound materials such as metal oxides, typically two precursors are necessary whose functional groups are compatible with each other to induce reactions at the substrate surface. The precursor choice depends on various factors, e.g., precursor reactivity, precursor evaporation temperature, thermal decomposition of the precursor, precursor handling, oxidation state of the element of interest in the precursor molecules, reaction by-products, and desired ALD reactor temperature. For V_xO_y deposition, thermal ALD and PEALD processes were reported [7,11]. Different β-diketonates, alkoxides, and alkylamides were applied as vanadium precursors in combination with water, oxygen, ozone, or oxygen plasma as oxidizing precursors. A detailed overview about the possible precursors and their combination for V_xO_y ALD is extensively described in a review article by Prasadam *et al.* [7]. In contrast to this previous work, we present an updated list of the processes used and focus our overview on their use for the fabrication of nanostructures based on V_xO_y.

Nevertheless, even though ALD offers excellent conformality in combination with precise thickness control and tunability of the material composition to tailor the materials' properties, the set of parameters to successfully perform coating of porous or 3D structures might differ significantly from the "standard" deposition onto planar substrates. What is more intriguing, is that the final properties of the deposited material have also been found to vary greatly, depending on the substrate or template. Thereby, this review article presents an overview about ALD-based V_xO_y nanostructures and their functional properties in catalysis, gas sensing, electrochemical energy storage, optics, or stimuli-induced properties switching for smart devices as schematically summarized in Fig. 1. As other comprehensive review articles – not specialized on ALD – in the literature already reported on the structure, properties, and applications of different vanadium oxide phases [1–6,8], this article only briefly summarizes the key characteristics of the relevant V_xO_y phases that are fabricated by ALD. Nevertheless, to establish the relation between ALD process-phase-properties, the properties of different ALD-based vanadium oxide phases are presented and the ALD processes that have been applied to fabricate V_xO_y nanostructures with different phases are discussed (Section 2). As our main focus is on V_xO_y nanostructures prepared via ALD, Section 3 of this article describes the properties and applications of ALD-based V_xO_y nanostructures classified according to the obtained V_xO_y phases. At last, existing challenges and future perspectives of V_xO_y nanostructures fabricated via ALD are presented in Section 4 and Section 5.

2. ALD of vanadium oxides

2.1. Vanadium oxide phases and properties

The unique properties of vanadium oxides (V_xO_y) depend on the vanadium atom oxidation state between + 5 and −3 whereby the range from + 5 to + 2 presents the most common oxidation states [1,4]. Thermodynamically stable phases can consist of both, single oxidation states such as divanadium trioxide (V_2O_3, oxidation state +3), vanadium dioxide (VO_2, oxidation state +4), and divanadium pentoxide (V_2O_5, oxidation state +5), as well as mixed oxidation states such as trivanadium pentoxide (V_3O_5, oxidation states +3 and +4) and trivanadium heptaoxide (V_3O_7, oxidation states +4 and +5) [1,4]. Aside from these phases, several metastable phases exist as depicted in the phase diagram in Fig. 2. The Magnéli series with the chemical formula V_nO_{2n-1} ($3 \leq n \leq 9$) and the Wadsley series with the formula V_nO_{2n+1} are examples of such metastable phases [1,18]. Moreover, mixtures of different phases are often observed for vapor phase deposited

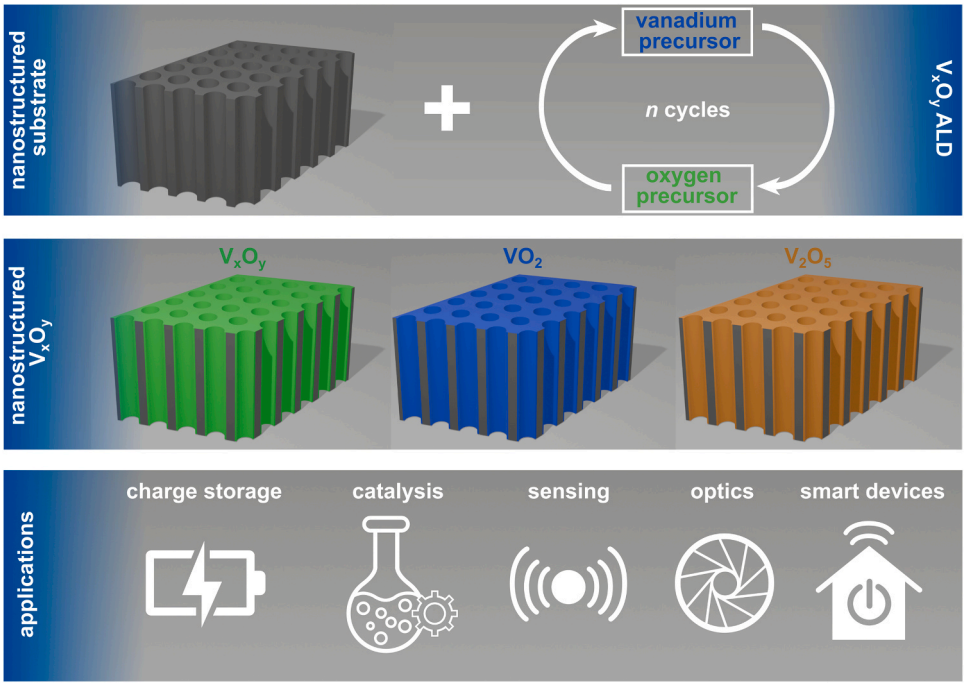

Fig. 1. Schematic overview of ALD-based fabrication of functional vanadium oxide nanostructures and their application fields.

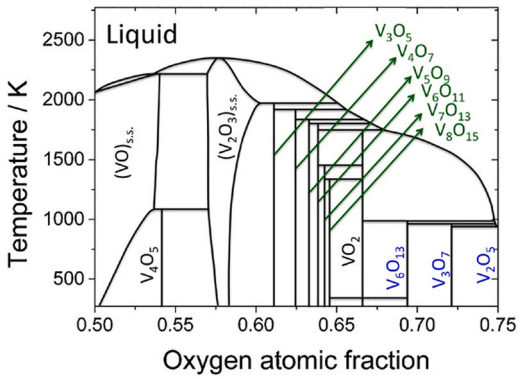

Fig. 2. Phase diagram of vanadium oxides. The combination of temperature and oxygen atomic fraction dictate the obtainable V_xO_y phases. Figure reprinted with permission.[2] Copyright 2014, Wiley-VCH.

as-synthesized vanadium oxides. Subsequently, they can be transformed into pure phases by different post-deposition procedures involving reduction or oxidation reactions [2,7,9]. A common practice is the thermal annealing of V_xO_y structures in controlled atmospheres and temperatures to obtain the desired phase(s) [1,2,4,7]. Nevertheless, fabricating phase pure V_xO_y structures is often challenging due to the complex thermodynamics in the V_xO_y system as shown in Fig. 2. Hence, different phases and oxidation states typically co-exist. V_2O_5 is the thermodynamically most stable phase which tends to form during storage at room temperature and ambient conditions [2]. Further, the vanadium oxidation state is very sensitive to slight changes of the surrounding atmosphere and temperature. Consequently, the more processing steps are required, the more intricate is the targeted preparation of a specific V_xO_y phase.

In general, vanadium oxides exhibit strong electron-electron and electron-lattice interactions [2,5,6,18]. Many vanadium oxides show an insulator-to-metal transition (IMT) accompanied by an alteration of the crystalline structure upon temperature increase. The IMT causes extensive changes in the (opto-)electronic properties. Thereby, films or nanostructures featuring an IMT are particularly interesting for applications as sensors, memory devices, and stimuli-responsive "smart" devices. For bulk V_xO_y phases, the IMT is reported at about 70 K, 130 K, 150 K, 160 K, 170 K, 240 K, 340 K, 450 K, and 530 K for V_8O_{15}, V_5O_9, V_6O_{13}, V_2O_3, V_6O_{11}, V_4O_7, VO_2, V_3O_5, and V_2O_5 phases, respectively [1,5,18]. From these, V_2O_3, V_2O_5, and VO_2 are the most explored phases and thus, described in details in the next paragraphs.

The V_2O_3 phase exists in a hexagonal corundum structure at room temperature [1,2]. During the IMT at 160 K, it transitions from an antiferromagnetic insulator with monoclinic symmetry to a paramagnetic metal with rhombohedral symmetry [2]. The IMT is caused by strong electron-electron interactions and lattice coupling of the Mott-Hubbard transition. V_2O_3 is often applied in catalysis or electrochemical energy storage [1,2].

Catalysis is also the main application for the V_2O_5 phase which has an orthorhombic layered crystal structure and is a wide bandgap semiconductor with a bandgap of 2.3 eV [1,18]. It shows a high catalytic activity and can also be utilized in gas sensing and optoelectronic devices [1]. Moreover, the layered structure renders it well-suited for electrochemical energy storage applications such as supercapacitors and batteries where electrolyte ions have to be intercalated in the material during the storage process [1]. Notably, V_2O_5 does not undergo a transition of the crystal structure at the IMT [18,19]. Instead, the IMT at 530 K is caused by changes in the electronic structure mostly at the materials' surface. Hence, thin films show a more pronounced IMT compared to bulk structures [18,19].

Meanwhile, the VO_2 phase presents a sharp and highly reversible IMT around 340 K where it transforms from a monoclinic type insulating phase to a rutile type metallic phase [1,2]. This structural transition is accompanied by significant changes in the (opto-)electrical properties. Especially the materials' conductivity increases by several orders of magnitude [18]. Based on the IMT close to room temperature, VO_2 can be applied in sensing, optics, and electrical switches [1,18].

Mixed V_xO_y and substoichiometric phases are often amorphous or only present nanocrystalline domains [1]. Since it has been reported that the mixture of different oxidation states can expand the functional performance compared to pure single phases, mixed phases can be beneficial for applications in catalysis and energy storage [1,9]. Mixed oxidation states also exist in vanadium oxides of the Magnéli and Wadsley series whereby the compounds from the Magnéli series – except V_7O_{13} – present IMTs [5]. However, as these phases are metastable, their practical applicability is limited.

2.2. ALD processes for vanadium oxide nanostructures

A variety of ALD processes for vanadium oxides have been developed over the last decade. We hereby forward the readers interested in the different types of vanadium precursors – namely β-diketonates, alkalines, and alkylamides – to the detailed review by Prasadam *et al.* [7]. Regardless of the precursor used, the majority of ALD processes result in amorphous materials revealing the need of post-deposition processing of the materials to obtain crystalline phases. A frequently used method for crystallization is thermal annealing in controlled atmosphere [7,20]. It has been reported that the V oxidation state in the precursor compound predetermines the achievable vanadium oxide phases after ALD deposition and subsequent annealing [7].

Applied ALD process for nanostructured V_xO_y are summarized in Table 1. The table is sorted by the final V_xO_y phase obtained after the complete fabrication process, i.e., ALD and post-deposition annealing. Additional to V_xO_y deposited on nanostructured templates – for instance carbon nanotubes (CNTs), anodic aluminum oxide (AAO), and powders – post-deposition annealing of films deposited on planar Si substrates which resulted in V_xO_y nanoparticles are also shown. Note, apart from this V_xO_y nanoparticle formation, ALD of V_xO_y thin films on planar substrates is not included in this manuscript. Further, all other processes result in thin films on nanostructured templates and this morphology remains stable upon post-deposition annealing.

The ALD process summary shows that VTOP is the most frequently used V precursor for nanostructured V_xO_y. Its evaporation temperature in the ALD process is varied between room temperature and 110 °C [25–32,34,35–37,48,49–51,57,58–61,63,64–74]. Also, different oxygen precursors can be combined with VTOP to result in V_xO_y deposition whereby H_2O is the most often used as visualized in Fig. 3. The plots include all V_xO_y phases obtained after ALD on nanostructures by utilizing different precursor combinations and deposition temperatures. Since the complex parameter space is multi-dimensional, only parts of it are depicted in the plots. The symbol size resembles the number of reported ALD processes utilizing the same analyzed parameters. Modifications of the process parameters, both ALD and post-deposition annealing, can lead to the generation of nanostructured V_xO_y [25–32], VOH [34], V_2O_3 [35], V_2O_4 [36,37], VO_2 [48–51], and V_2O_5 [50,57–61,63,64–74] phases starting from VTOP plus oxidizer.

Although VTOP is widely used, significant differences in the utilization of V precursors are observed for ALD of nanostructured VO_2. ALD of this phase has been intensively studied in planar substrates due to the interesting electronic and optic properties based on the IMT [2,7]. However, deposition of nanostructured VO_2 appears to be more challenging since it is not the thermodynamically most stable phase. Some studies report on the deposition of thin films on planar substrates followed by annealing to form VO_2 nanoparticles [20,38,41,43,44,48,49]. Nanoparticle formation is reported for TDMAV, TEMAV, and VTOP as V precursors in combination with H_2O, O_3, or O_2 plasma as oxygen precursors. Even though the VO_2 nanoparticles present IMT properties, such ALD process cannot be used to conformally coat nanostructured

Table 1
Summary of ALD processes and post-deposition annealing conditions for nanostructured V_xO_y. *Final V_xO_y phase* denotes the resulting crystallographic phase after ALD and post-deposition annealing. All presented V_xO_y ALD processes on nanostructured substrates lead to thin film deposition and the thin film morphology is preserved during the complete processing. For V_xO_y ALD on planar Si included in this table, the thin films transform to nanoparticles in the post-deposition annealing steps.

Final V_xO_y phase	Substrate	ALD process					Phase after ALD	Post-deposition annealing			Ref.
		ALD mode	Vanadium precursor	Oxygen precursor	Deposition temperature /°C	GPC /Å		Atmosphere	Temperature /°C	Dwell time	
V_xO_y	Graphene fibers	Thermal ALD, flow mode	TDMAV @ 90 °C	H_2O	150	1.2	Amorphous V_xO_y				[21]
V_xO_y	Al_2O_3 or SiO_2 particle powders	Thermal ALD, flow mode	$VO(acac)_2$ @ 170 °C	air	180		V_xO_y				[22]
V_xO_y	Graphene oxide	Thermal ALD, flow mode	$VOCl_3$	H_2O	60		V_xO_y	O_3	150	10 days	[23]
V_xO_y	Si nanowires	Thermal ALD, flow mode	$VOCl_3$	H_2O	650		V_xO_y				[24]
V_xO_y	AAO	Thermal ALD, flow mode	VTOP	H_2O_2 + H_2O			V_xO_y	Air	500	2 h	[25]
V_xO_y	SiO_2 and TiO_2 particle powders	Thermal ALD, flow mode	VTOP	O_2	110 (SiO_2 particles), 90 (TiO_2 particles)			O_2	500	11 h	[26]
V_xO_y	SBA−15 and FDU−15	Thermal ALD	VTOP @ 40 °C	H_2O	150		Amorphous V_xO_y				[27]
V_xO_y	Activated carbon and carbon onions	Thermal ALD, flow mode	VTOP @ 45 °C	H_2O	180		V_xO_y				[28]
V_xO_y	Al_2O_3 powder	Thermal ALD, flow mode	VTOP @ 45 °C	H_2O	150		V_xO_y	Air	600	6 h	[29]
V_xO_y	CNTs	Thermal ALD, flow mode	VTOP @ 45 °C	H_2O @ 100 °C	170−190	1.0	V_xO_y				[30]
V_xO_y	Al_2O_3 powder	Thermal ALD, flow mode	VTOP @ 50 °C	H_2O @ 25 °C	100		V_xO_y	Air	550	4 h	[31]
V_xO_y	CNTs	Thermal ALD, exposure mode	VTOP @ 70 °C	H_2O	130−170		V_xO_y				[32]
V_xO_y	TiO_2 and TiO_2-coated SiO_2 particle powders	Thermal ALD, flow mode	VTOP @ 90 °C	O_2	90			O_2	500	11 h	[33]
VOH	Porous carbon	Thermal ALD, exposure mode	VTOP @ 70 °C	H_2O	150	0.4	V_2O_5	Air	1) 900 2) RT	1) 1 min 2) 30 days	[34]
V_2O_3	Porous carbon	Thermal ALD, exposure mode	VTOP @ 70 °C	H_2O	150	0.4	V_2O_5	Air	900	1 min	[35]
V_2O_4	CNTs	Thermal ALD, exposure mode	VTOP @ 80−90 °C	CH_3COOH @ 40 °C	200	0.4	Amorphous V_2O_4	Air	150−300		[36]
V_2O_4	CNTs	Thermal ALD, exposure mode	VTOP @ 90 °C	CH_3COOH @ 40 °C	200	0.4	Amorphous V_2O_4	Air	150		[37]
VO_2	Planar Si	Thermal ALD, flow mode	TDMAV	H_2O or O_3	50−120	0.3 (H_2O) and 0.45 (O_3)	Amorphous V_xO_y	N_2	800	2 h	[38]
VO_2	PS opals	Thermal ALD, exposure mode	TDMAV @ 70 °C	H_2O	95	0.56	V_xO_y	vacuum N_2 with low O_2 partial pressure	390 425	6 h 20 min	[39]
VO_2	Si nanowires	Thermal ALD, exposure mode	TDMAV @ 70 °C	H_2O	150	0.56	V_xO_y	N_2 with low partial pressure O_2	450	10 min	[40]

(*continued on next page*)

Table 1 (*continued*)

Final V_xO_y phase	Substrate	ALD process					Phase after ALD	Post-deposition annealing			Ref.
		ALD mode	Vanadium precursor	Oxygen precursor	Deposition temperature /°C	GPC /Å		Atmosphere	Temperature /°C	Dwell time	
VO_2	SiO_2- or Al_2O_3-coated planar Si	Thermal ALD, flow mode	TEMAV	O_3	100–150	0.1–0.14	Amorphous V_2O_5	N_2 with low O_2 partial pressure	Up to 500	5–40 min	[41]
VO_2	Si micropillars	Thermal ALD, exposure mode	TEMAV	O_3	150		Amorphous VO_2	He with low partial pressure O_2	450		[42]
VO_2	Planar Si	Thermal ALD, flow mode	TEMAV	O_3	150		Amorphous VO_2	He with low O_2 partial pressure	Up to 820		[20]
VO_2	Planar Si	Thermal ALD	TEMAV	H_2O	150	0.5	Amorphous VO_2	N_2 with low O_2 partial pressure	540		[43]
VO_2	Planar Si	PEALD	TEMAV @ 80 °C	O_2 plasma	170		V_xO_y	Vacuum	250–700	1 h	[44]
VO_2	ITO nanorods	Thermal ALD, flow mode	$V(amd)_3$ @ 190 °C	$H_2O_2 + H_2$	200	0.31		H_2	350	5 h	[45]
VO_2	Si nanowires	Thermal ALD, flow mode	$VOCl_3$	H_2O	650		VO_2 and V_2O_5	H_2	500	8 h	[46]
VO_2	SiO_2 opals	Thermal ALD, flow mode	$VOCl_3$	H_2O	490						[47]
VO_2	Planar Si	Thermal ALD	VTOP	H_2O	150		V_xO_y	Ar	600	4 h	[48]
VO_2	Planar Si	Thermal ALD	VTOP	H_2O	150			Ar	550	4 h	[49]
VO_2	Patterned SiO_2	Thermal ALD, flow mode	VTOP @ 40 °C	H_2O	135	0.3	Amorphous V_xO_y	Forming gas	500	1 h	[50]
VO_2	Patterned SiO_2	Thermal ALD, flow mode	VTOP @ 60 °C	H_2O @ 60 °C	200	0.16	Amorphous V_xO_y	Ar	550	4 h	[51]
V_2O_5	TNTs	Thermal ALD, flow mode	TDMAV	H_2O	200	0.68	V_2O_5				[52]
V_2O_5	CNTs	Thermal ALD, flow mode	TEMAV	H_2O	100		V_xO_y	Air	325	1 h	[53]
V_2O_5	Al_2O_3, TiO_2, or SiO_2 powder		$VO(acac)_2$	Air	170			Air	500	16 h	[54]
V_2O_5	P25 powder	Thermal ALD, flow mode	$VO(acac)_2$ @ 170 °C	Air	180			Air	500	4 h	[55]
V_2O_5	Planar Si	Thermal ALD, flow mode	$VO(thd)_2$ @ 125 °C	O_3	215	0.5	V_2O_5				[56]
V_2O_5	Graphene oxide	Thermal ALD, flow mode	$VOCl_3$	H_2O	60		V_2O_5	Air	550	6.5 h	[23]
V_2O_5	AAO	Thermal ALD	VTOP	O_3	170	1.0	V_2O_5				[57]
V_2O_5	AAO	Thermal ALD	VTOP	O_3	170	0.33	V_2O_5				[58]
V_2O_5	Tobacco mosaic virus	Thermal ALD, flow mode	VTOP	O_3	170	0.3	Crystalline V_2O_5				[59]
V_2O_5	CNTs	Thermal ALD, flow mode	VTOP	H_2O	150	0.8	Amorphous V_2O_5				[60]
V_2O_5	CNT sponge		VTOP	H_2O	120		Amorphous V_2O_5				[61]
V_2O_5	AAO	Thermal ALD, flow mode	VTOP	H_2O_2	100		V_2O_5				[62]
V_2O_5	Patterned SiO_2	Thermal ALD, flow mode	VTOP @ 40 °C	H_2O	135	0.3	Amorphous V_xO_y	Air	500	1 h	[50]

(*continued on next page*)

Table 1 (*continued*)

Final V_xO_y phase	Substrate	ALD process					Phase after ALD	Post-deposition annealing			Ref.
		ALD mode	Vanadium precursor	Oxygen precursor	Deposition temperature /°C	GPC /Å		Atmosphere	Temperature /°C	Dwell time	
V_2O_5	Planar Si	Thermal ALD, flow mode	VTOP @ 45 °C	H_2O	105	0.15		Air	250–600	2 h	[63]
V_2O_5	Mesoporous ITO nanocrystal film	Thermal ALD, flow mode	VTOP @ 45 °C	H_2O or O_3	120 (H_2O) or 170 (O_3)	0.2–0.28		O_2	200–450	60 s	[64]
V_2O_5	Activated carbon	Thermal ALD, flow mode	VTOP @ 45 °C	H_2O		1.3	V_2O_5				[65]
V_2O_5	AAO	Thermal ALD, flow mode	VTOP @ 45 °C (boost)	O_3	170–185	0.27	V_2O_5				[66]
V_2O_5	Activated carbon	Thermal ALD, exposure mode	VTOP @ 45 °C (boost)	H_2O	125–175	0.2–0.3	Amorphous V_2O_5				[67]
V_2O_5	Activated carbon	Thermal ALD, exposure mode	VTOP @ 45 °C (boost)	H_2O	150		V_2O_5	Air	200–300	1 h	[68]
V_2O_5	Mesoporous carbon	PEALD	VTOP @ 45 °C (boost)	O_2 plasma	180		V_2O_5				[69]
V_2O_5	CNTs	Thermal ALD, flow mode	VTOP @ 45 °C (boost)	H_2O	120	0.17	V_2O_5				[70]
V_2O_5	CNTs	Thermal ALD, flow mode	VTOP @ 55 °C	H_2O	150	0.7	V_2O_5				[71]
V_2O_5	CNFs	Thermal ALD, exposure mode	VTOP @ 80–90 °C	CH_3COOH @ 40 °C	200	0.4	Amorphous V_2O_5	Air	150–300		[72]
V_2O_5	SiO_2 particle powder	Thermal ALD, flow mode	VTOP @ 90–110 °C	O_2	90–120			O_2	500	11 h	[73]

Abbreviations: tetrakis dimethylaminovanadium (TDMAV), tetrakis ethylmethylaminovanadium (TEMAV), vanadium oxy-tri-isopropoxide (VTOP), vanadium oxytrichloride ($VOCl_3$), vanadyl acetylacetonate ($VO(acac)_2$), tris(*N,N'*-diisopropylacetamidinate)vanadium ($V(amd)_3$), vanadyl bis(2,2,6,6-tetramethyl-3,5-heptadionate) ($VO(thd)_2$), carbon nanotube (CNT), carbon nanofiber (CNF), polystyrene (PS), anodic aluminum oxide (AAO), indium tin oxide (ITO).

substrates with VO_2. Upon the phase conversion the structure might collapse due to the particle formation (in case of templates) or present discontinuity due to particle formation-induced film breakdown. Thus, precise tailoring of both, the ALD process and the post-deposition annealing, is required to maintain the continuous nature of the VO_2 coatings on the nanostructured substrates after annealing. Such continuous and conformal VO_2 nanostructures – often merely obtained after post-processing – have been reported for ALD processes with TDMAV [39,40], TEMAV [42], $V(amd)_3$ [45], $VOCl_3$ [46,47], or VTOP [50,51,74]. Except for TEMAV and $V(amd)_3$, all V precursors were combined with H_2O as oxygen precursor. The exact annealing conditions to obtain VO_2, namely atmosphere, temperature, and duration, depend on the utilized ALD parameters and resulting V_xO_y phases after ALD deposition. While the TDMAV, TEMAV, $V(amd)_3$ and VTOP processes are operated at low to moderate deposition temperatures of 95–150 °C, 150 °C, 200 °C, and 135–200 °C, respectively, the $VOCl_3$ based process uses way higher deposition temperatures between 490 °C and 650 °C which limits its applicability for some substrates. Continuous coatings are reported to be retained when post-deposition annealing temperatures are below 500 °C [39,40,42,46,50,74]. Although a publication by Premkumar *et al.* in 2012 reported the deposition of amorphous V_2O_5 from TEMAV and O_3 on planar substrates [41], later studies demonstrated that utilization of TEMAV can directly result in amorphous VO_2 phase after thermal ALD as confirmed by XPS and XRD measurements [20,42–44]. The V cation is already present in the V^{4+} state in TEMAV which can be beneficial for the direct deposition of VO_2 in the ALD process. However, there are controversial observations regarding the oxygen precursor. Peter *et al.* attributed the direct deposition of VO_2 to their utilization of H_2O with less oxidizing strength [43] in contrast to the study by Premkumar *et al.* whom used O_3 resulting in V_2O_5 deposition [43]. Nevertheless, studies by Rampelberg *et al.* and Mattelaer *et al.* reported direct VO_2 deposition for the combination of TEMAV and O_3 [20,42].

Besides the precursor combinations and deposition temperatures, also the utilized substrate material and nanostructures affect the resulting V_xO_y phases. Fig. 4 represents the correlations between V_xO_y phases after ALD and after annealing and the utilized substrates. For example, V_xO_y ALD on carbon nanostructures leads to V_xO_y or V_2O_5 after ALD which was usually not exposed to post-deposition annealing. Si- and SiO_2-based substrates can be utilized to fabricate V_xO_y, VO_2, and V_2O_5 nanostructures after ALD and annealing. While most processes result in V_xO_y or not specified phases after ALD, the utilization of planar Si or Si micropillars can lead to direct VO_2 growth. Here, it has to be noted that the processes on planar Si substrates result in VO_2 nanoparticles after the post-deposition annealing. Al_2O_3 and TiO_2 nanostructures are coated with either V_xO_y, V_2O_5, or not specified phases after ALD which remain as V_xO_y or can be transformed into V_2O_5 based on the reported publications.

Moreover, the post-deposition annealing conditions in combination with the utilized substrate are crucial for determining the final V_xO_y

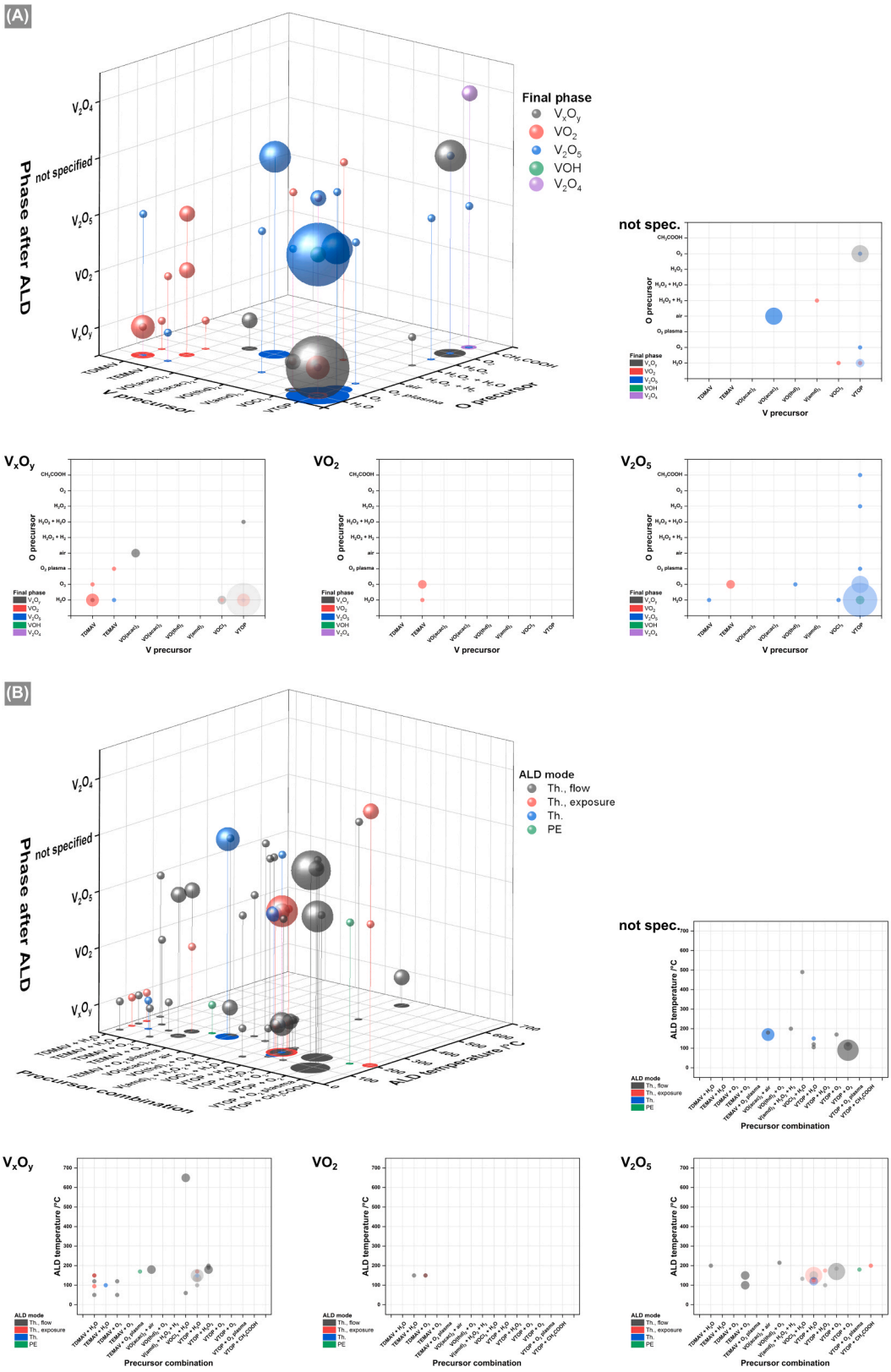

Fig. 3. Parts of the V_xO_y ALD parameter space to visualize the relationships between ALD parameters, as-deposited V_xO_y phases, – phase after ALD – and the final phases obtained after post-deposition annealing. The size of the data points resembles the counts of publications reporting these parameter combinations. The 3D plots depict the dependencies between (A) V precursor, O precursor, phase after ALD, and final phase after annealing and (B) precursor combination, ALD temperature, phase after ALD, and ALD mode, respectively. Moreover, the most reported phases after ALD in the 3D plots are also summarized in the 2D plots for improved visibility.

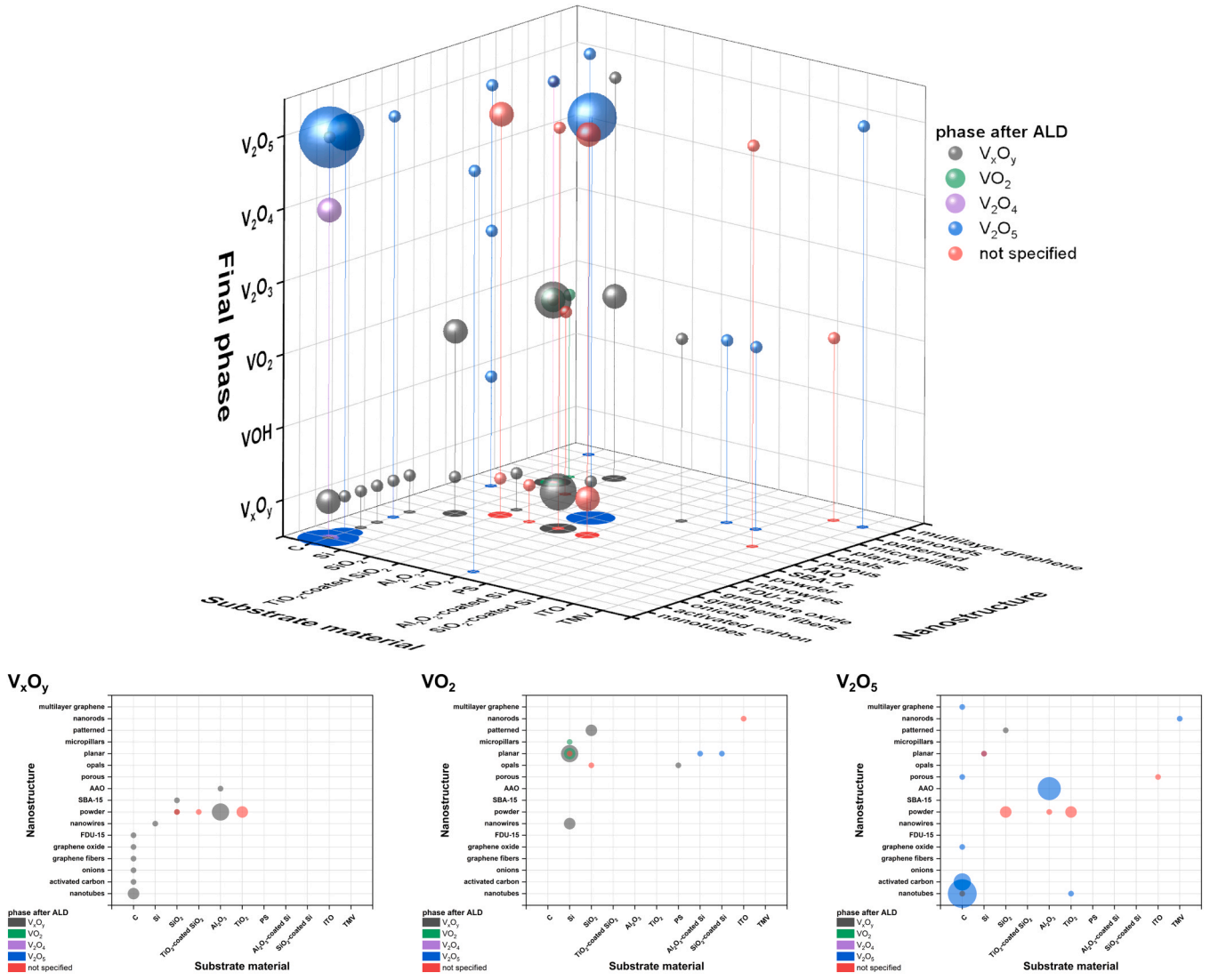

Fig. 4. Correlation of V_xO_y phases after ALD and after annealing, i.e., final phase, depending on the substrate material and nanostructure. The size of the data points displays the counts of publications utilizing the same analyzed parameters. The 3D plots depict the dependencies between substrate material, nanostructure, final phase, and phase after ALD. The substrate parameters for the most frequently obtained final phases are also shown in the 2D plots for improved visibility.

phase as expected from the phase diagram. V_xO_y-coated carbon-based nanostructures are mostly exposed to air as annealing atmosphere resulting in V_2O_4 or V_2O_5 phases as shown in Fig. 5. Annealing in air can also be used for fabricating V_2O_3 or retaining as-deposited V_xO_y phases. Similarly, post-deposition annealing in O_2 results in V_2O_5 coatings on a porous ITO substrate while films deposited on powders from SiO_2, TiO_2-coated SiO_2, or TiO_2 transform into V_2O_3, V_xO_y, and V_xO_y, respectively. VO_2 as final phase after annealing is obtained using most different types of atmospheres, namely, vacuum, Ar, N_2, H_2, forming gas, He with low O_2 partial pressure, and N_2 with low O_2 partial pressure. In contrast to the annealing atmosphere, the temperature is less important for determining the final V_xO_y phase of ALD-based V_xO_y nanostructures within the reported temperature range as depicted in Fig. 5B. Post-deposition annealing for crystallization of amorphous as-deposited ALD films is in general sensitive to many different parameters as the crystallization typically depends on the atmosphere, temperature, surface groups and binding energies to the substrate material, and deposited material thickness [75–78]. Especially the latter one is a crucial but also very complex parameter, because confinement of the film dimensions on the nanometer scale significantly alters their crystallization behavior. Moreover, nanostructuring not only leads to confinement effects but also increases the surface and interface areas of the material to its' surrounding. Hence, the influence of surface groups of the deposited V_xO_y films and binding energies to the underlying substrates increases and can alter the required annealing. Accordingly, the post-deposition annealing conditions are strongly dependent on the inherent properties of ALD-based V_xO_y films in combination with their nanostructured substrate.

In summary, nanostructured substrates have been functionalized with various V_xO_y phases. Preparation of one specific phase requires accurate control of the ALD process – including the precursor type (see Table 1) – and the post-deposition annealing. Hence, several parameter combinations were explored in literature and different process routes have been reported to result in the same V_xO_y phase. This presents an opportunity in terms of post-processing options, while simultaneously indicating the variability existing in the ALD-processing and post-deposition treatments of vanadium oxides' nanostructures. On the one hand, carefully choosing the ALD precursor combination and ALD conditions is a prerequisite for successful nanostructure functionalization with a desired V_xO_y phase. On the other hand, the variety of processes for specific phases allows to select those suitable for the respective substrate.

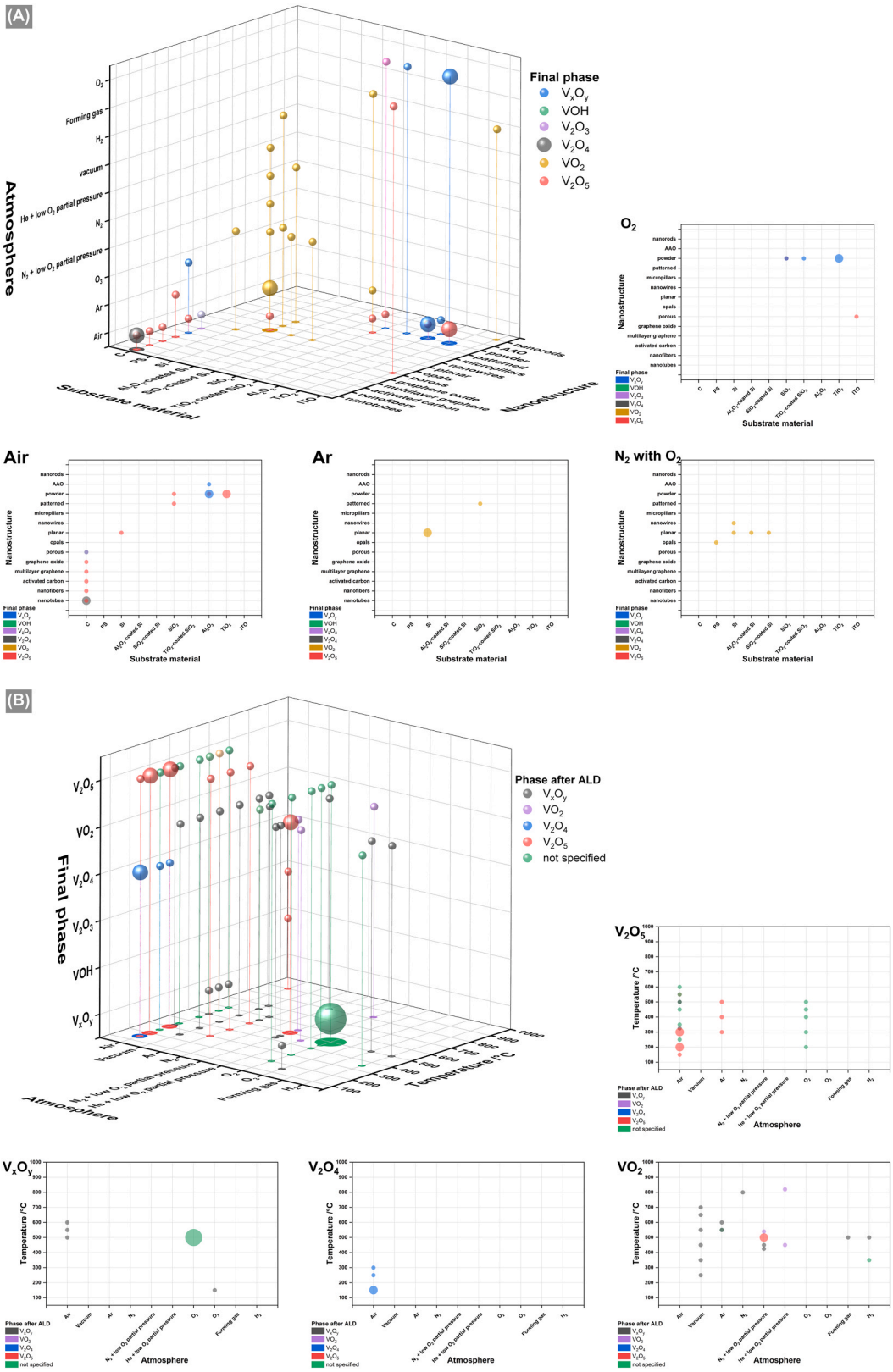

Fig. 5. Post-deposition annealing parameter space to visualize the relationships between annealing conditions, V_xO_y phases after ALD, and the final phases obtained after the annealing. The size of the data points resembles the counts of publications reporting these parameter combinations. The 3D plots depict the dependencies between (A) substrate material, nanostructure, annealing atmosphere, and final phase and (B) atmosphere, annealing temperature, final V_xO_y phase, and phase after ALD, respectively. Moreover, the most reported atmospheres and final phases in the 3D plots of (A) and (B) are depicted in the respective 2D plots for improved visibility.

3. Properties and applications of ALD-based vanadium oxide nanostructures

Applications of ALD-based V_xO_y nanostructures are reported in the following paragraphs. The named V_xO_y phases obtained after post-deposition annealing are at least the dominating phases if multiple phases are still present after the complete fabrication processes. Nevertheless, several publications report about phase purity according to lab-based X-ray diffraction measurements.

3.1. V_2O_4

ALD-based V_2O_4 nanostructures were reported for NO_2 sensing [36,37]. V_2O_4-coated CNTs presented a faster response for NO_2 sensing than their uncoated counterparts while the responses to interfering gases such as CO, C_2H_5OH, and NH_3 were negligible. A publication by Willinger *et al.* reports an inverted resistance sensing behavior for V_2O_4-coated CNTs compared to the uncoated CNTs (Fig. 6C) [37]. While the uncoated structures show a decreasing resistance upon NO_2 exposure according to a p-type semiconducting behavior, the resistance of V_2O_4-coated CNTs increases corresponding to n-type behavior. Further, they reported a slightly higher sensitivity for a 2 nm thick V_2O_4 coating compared to a 4.5 nm coating. Another study by Willinger *et al.* demonstrates that also the post-deposition annealing temperature affects the V_2O_4-CNT sensor response as shown in Fig. 6B [36]. Up to 200 °C the V_2O_4 coating is likely oxidized to other phases causing an increased sensor response. Meanwhile, higher annealing temperatures seem to lead to the oxidation of the CNTs resulting in reduced sensing performance.

3.2. VO_2

Fundamental studies for the fabrication of ALD-based VO_2 nanostructures revealed that V_xO_y thin films deposited on planar Si substrates can be transformed into VO_2 nanoparticles (NPs) by post-deposition annealing [20,38,43,44,48,49]. *In situ* XRD during thermal annealing of V_xO_y was investigated by Rampelberg *et al.* (Fig. 7A), who showed the formation of VO_2 upon annealing in He atmosphere with a low O_2 partial pressure at temperatures up to 820 °C [20]. While the film thickness had no significant effect on the crystallization onset, it was crucial for the agglomeration into NPs which occurred for thicknesses below 11 nm at 450 °C. Increasing the annealing temperature in the range of 450 °C to 820 °C led to the NPs agglomeration of films with increased thicknesses up to 33 nm as schematically summarized in Fig. 7A. Notably, after annealing of the thin films to 820 °C and subsequent cooling to room temperature, all structures remained in NP shape as shown in the SEM images. Similarly, Peter *et al.* observed agglomeration of V_xO_y thin films with thicknesses up to 6 nm into VO_2 NPs during post-deposition annealing at 540 °C in N_2 atmosphere with a low O_2 partial pressure [43]. The NP sizes increased with the ALD-deposited film thicknesses.

In 2018, Wang *et al.* reported the presence of minor V_2O_5 content at the surface of VO_2 NPs after their formation by annealing-induced agglomeration from ALD-deposited thin films [48]. Local irradiation of the NPs with a 532 nm laser beam resulted in photooxidation into V_2O_5 phase for which surface adsorbed oxygen was required (Fig. 7B). A consecutive study from the same group investigated possibilities to suppress the oxidation of VO_2 during Raman measurements [49]. Since oxygen molecules adsorbed at the VO_2 NP surface are crucial for photooxidation, performing Raman measurements in N_2 atmosphere

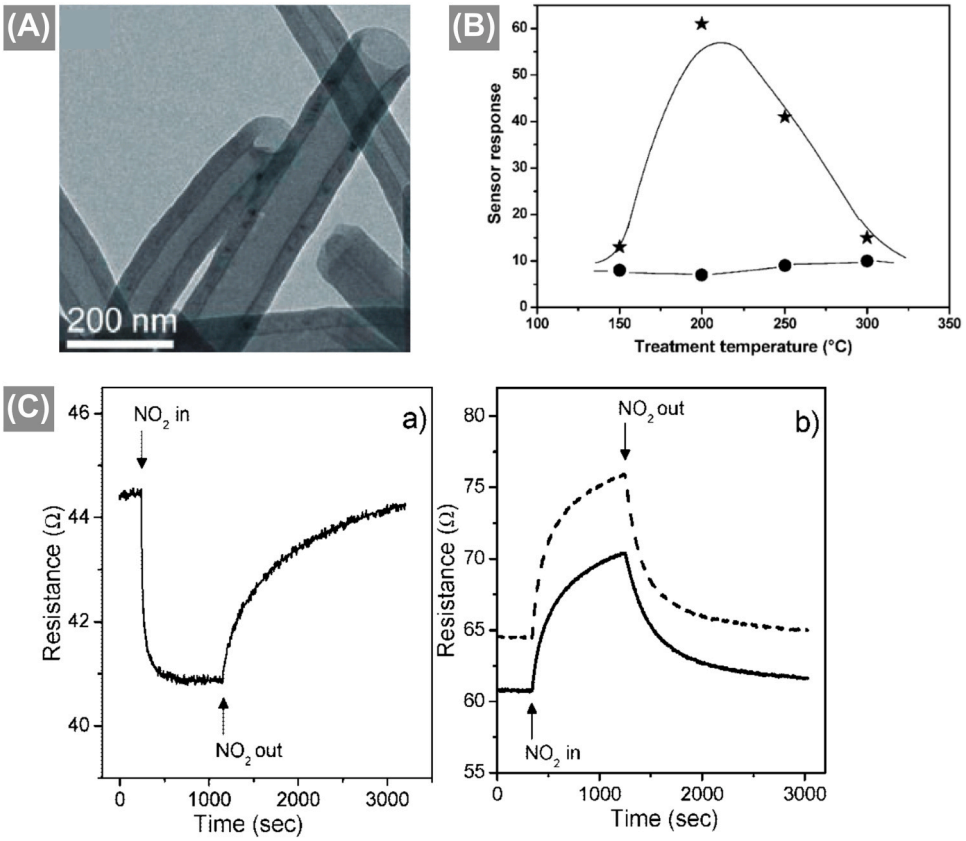

Fig. 6. (A) TEM image of V_2O_4-coated CNTs. (B) The gas sensor response depends on the annealing temperature for V_2O_4-coated CNTs (stars) compared to uncoated CNTs (circles). (C) Gas sensing performance improves with V_2O_4 coating and the resistance increases for (a) uncoated CNTs while it decreases for (b) V_2O_4-coated CNTs according to p-type and n-type semiconducting behavior, respectively. In (b), sensing behavior of CNTs coated with 4.5 nm V_2O_4 (solid line) and 2 nm V_2O_4 (dashed line) are shown. Figures adapted with permission [36,37]. (A) and (C) copyright 2008, American Chemical Society, (B) copyright 2009, Royal Society of Chemistry.

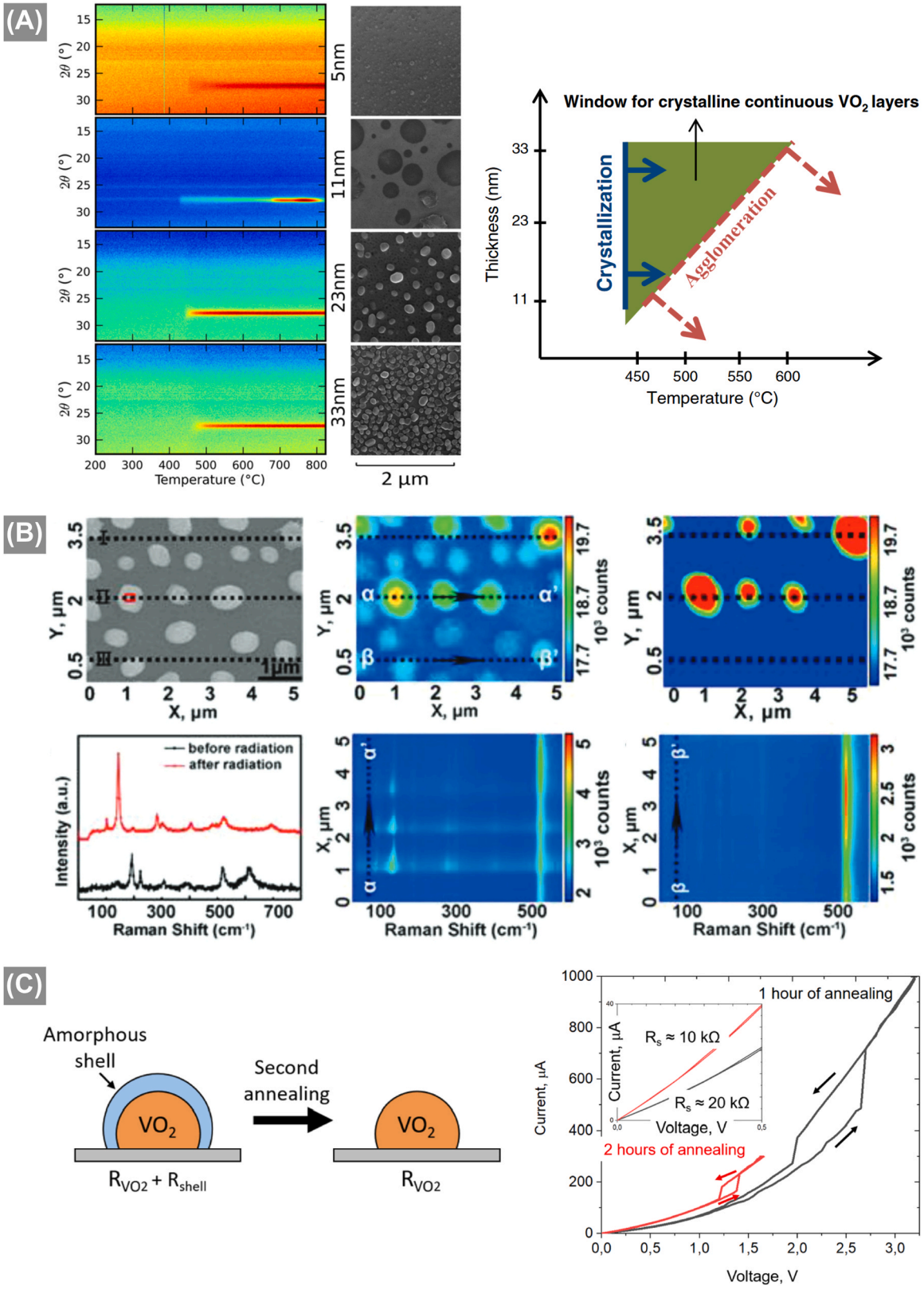

Fig. 7. VO_2 NPs formed by ALD and post-deposition annealing. (A) In situ XRD studies during post-deposition annealing of vanadium oxide thin films with different thicknesses and SEM images of the agglomerated VO_2 NPs after the annealing process. The right graph shows the crystallization regimes depending on the film thickness and annealing temperature. Figures reprinted with permission [20]. Copyright 2014, Elsevier. (B) SEM image, Raman spectrum, and Raman intensity maps of VO_2 NPs and formed V_2O_5 shells after local laser beam irradiation. Figure reprinted with permission [48]. Copyright 2018, Wiley-VCH. (C) Removal of an amorphous V_2O_5 shell on VO_2 NPs is achieved by a second annealing step and leads to a reduction of the threshold voltage for resistive switching of the NPs. Figures reprinted with permission [44]. Copyright 2025, Elsevier.

could avoid the oxidation. Additionally, overcoating the VO_2 NPs with a thin TiO_2 layer by ALD was another possibility to suppress the VO_2 oxidation during laser beam irradiation even in ambient atmosphere [49]. VO_2 nanostructures are of great interest due to their IMT at relatively low temperatures around 68 °C and the associated switching of optical and electronic properties. The switching behavior of VO_2 NPs formed by agglomeration was studied by Peter *et al.* [43]. The expected IMT around 68 °C was confirmed for VO_2 NPs with diameters of 10–20 nm by in situ XRD and spectroscopic ellipsometry, respectively. Meanwhile, Kapoguzov *et al.* also investigated the properties of ALD-based VO_2 NPs [44]. They reported the only PEALD process for subsequent VO_2 NP formation. With this PEALD process, increasing the VO_2 content in the as-deposited thin film via decrease of the oxygen content during the ALD plasma pulse led to NP size reduction – associated with an increase in NP density. Voltage-induced resistive switching was observed for the VO_2 NPs, but it was hindered by an amorphous V_2O_5 shell on the VO_2 NPs. The shell could be removed by crystallization in a second annealing step at 650 °C for 1 h. Prolonging the second annealing to 2 h significantly reduced the required threshold voltage for the resistive switching as shown in Fig. 7C. Further, Kapoguzov *et al.* estimated the phase transition time to be below 50 ns and the required energy to 150 fJ. In addition, switching of the VO_2 NPs was reproducible for 10^{10} cycles which renders them suitable for resistive switching devices.

Besides VO_2 NP formation, conformal coating of previously nanostructured substrates with VO_2 by ALD is especially interesting for generating switchable nanostructures. For example, Song *et al.* fabricated VO_2 films on patterned SiO_2 substrates [50]. A 10 nm VO_2 film prepared by ALD and post-deposition annealing in forming gas showed a stable voltage-induced IMT for 20 cycles. Recently, Peng *et al.* demonstrated the coating of Al_2O_3-functionalized Si nanowires (NWs) with VO_2 by ALD and post-deposition annealing for 3D memristor devices as depicted in Fig. 8A [40]. Voltage-induced resistive switching occurred at lower threshold voltages than in a non-structured thin film device and it was very sensitive to the operating temperature.

Since the IMT is also associated with a change of the optical properties, applications of VO_2 nanostructures in optics were reported. Povey *et al.* infiltrated SiO_2 opals with V_xO_y by ALD and transformed the phase into pure VO_2 by post-deposition annealing [47]. This photonic crystal (PhC) featured a photonic stopband (PSB) – a spectral range in which electromagnetic radiation cannot propagate through the structure – in the visible region of the electromagnetic spectrum. The PSB of the VO_2-coated SiO_2 opal shifted towards lower wavelengths with increasing temperature due to the IMT of VO_2 that consequently alters the material intrinsic optical properties. A similar structure was reported by Peng *et al.* in 2024, however, coating a polymeric template instead of a SiO_2 template. After vapor-phase removal of the polymer template, VO_2 inverse opal PhCs were obtained [39]. The VO_2 PhC showed a PSB at 1.49 μm as depicted in Fig. 8B. The post-deposition annealing process had to be adapted for the nanostructured substrate compared to a planar thin film by prolonging the annealing duration demonstrating the challenges associated to the fabrication of VO_2 nanostructures in comparison to planar thin films. The PSB position of the resulting VO_2 PhC switched to a lower wavelength of 1.03 μm above the IMT at about 60–70 °C and was reversibly switched back to its original position during cool down of the PhC structure. In addition, Wang *et al.* reported about the antireflective properties of ALD-based VO_2 coatings onto patterned SiO_2 [51]. The structure featured a lower reflectivity than the patterned SiO_2 without V_xO_y coating (Fig. 8C). Furthermore, annealing of the as-deposited V_xO_y film to VO_2 improved the antireflective properties to less than 2% reflection in the range from 650 nm to 1335 nm. The formation of small cracks in the VO_2 layer during annealing led to multiple light scattering in the film which further improved light trapping by the structure.

VO_2-coated Si pillars were also tested as 3D electrodes for lithium ion batteries (LIBs) [42]. The structures demonstrated very high volumetric capacities of 130 μA/h whereby the amorphous VO_2-coated electrodes showed higher performances than crystalline VO_2-coated electrodes. Furthermore, the capacity of the 3D structured electrode was significantly increased compared to their planar counterparts with the same VO_2 film thickness as shown in Fig. 8D.

3.3. V_2O_5

Nanoparticle formation during post-deposition annealing of ALD-deposited thin films was also observed for V_2O_5. Groult *et al.* systematically investigated the thickness dependence of the NP formation in thin films already in 2006 [63]. Starting from a continuous thin film, elongated V_2O_5 NPs emerged and grew further with increasing annealing temperature from 250 °C to 600 °C as shown in Fig. 9A. An initial film thickness of 15 nm resulted in larger V_2O_5 structures than a 5 nm thick film while the particle density after annealing to 600 °C was almost the same. Such elongated NPs were not observed for VO_2 NPs and can be related to preferential growth of the V_2O_5 phase according to the orthorhombic crystal structure.

AAO was used as a nanostructured substrate to characterize an O_3-based ALD process resulting in the growth of crystalline V_2O_5 [66]. In 2017, Song *et al.* reported that nanostructured V_2O_5 prepared by ALD and post-deposition annealing exhibited instable hysteresis behavior upon voltage sweeping [50]. No reproducible resistive switching was observed in contrast to the VO_2-based device which was discussed in the previous subsection. Application of V_2O_5-coated carbon nanofibers (CNFs) for NO_2 sensing revealed an influence of the annealing temperature on the sensing performance [72]. Additionally, another work from the same group investigated the sensing performance of V_2O_4-coated CNTs. In this study, Santangelo *et al.* figured out that as-deposited films consisted of V_2O_4 and transform into V_2O_5 as thermodynamically most stable phase during storage in air over several days or by post-deposition annealing in ambient air [72]. The highest sensor response was observed for structures annealed at 220 °C and the performance decreased at higher temperatures due to partial oxidation of the CNFs and V_2O_5 island growth. Meanwhile, Baishya *et al.* explored the effect of ultra-thin V_2O_5 coatings of titanium nanotubes (TNTs) on the growth of MG−63 cells [52]. The cell growth on TNTs with 15 nm diameter was not affected by the V_2O_5 coating (Fig. 9B). However, less cells grew on TNTs with a larger diameter of 30 nm and 100 nm compared to their respective uncoated counterparts due to a cytotoxic effect of the V_2O_5 coating on the investigated MG−63 cells. This behavior was independent of the crystallinity of the TNTs, namely amorphous or crystalline, for all investigated structures. The TNT's surface roughness decreases with increasing diameter which affected cell adhesion and growth. Further, the reduced cell growth on V_2O_5-coated TNTs was accompanied by decreased cell elongation. This indicated reduced cell attachment and adhesion to the surface caused by the V_2O_5 coating.

ALD-based V_2O_5 nanostructures were also studied for application as catalysts for the oxidation of cyclohexane [62] and o-xylene [54], oxidative dehydrogenation of propane [55], and their ammonia adsorption capabilities [73]. Only few ALD cycles were applied in these publications to deposit vanadium oxide on the support materials. In this context, Gervasini *et al.* conducted only one ALD half-cycle with VO $(acac)_2$ as precursor and transformed the chemisorbed molecules to V_2O_5 by calcination in air at 500 °C for 16 h [54]. Kazerooni *et al.* applied a similar process by performing the $VO(acac)_2$ half-cycle at 170 °C followed by the air half-cycle at 350 °C [55]. However, they used up to three ALD cycles and after finishing the V_xO_y ALD cycles, the samples were annealed in air at 500 °C for 4 h. It was found by three reports that ALD-deposited V_2O_5 catalysts achieved higher dispersion on the catalyst support, higher acidity and thus, also higher catalytic activities than wet-impregnated samples [54,55,73].

The majority of ALD-based V_2O_5 nanostructures were applied in the field of energy storage. CNTs [53,60,61,70,71], AAO [57,58], tobacco mosaic virus (TMV) [59], and planar Si [56] were used as substrates for

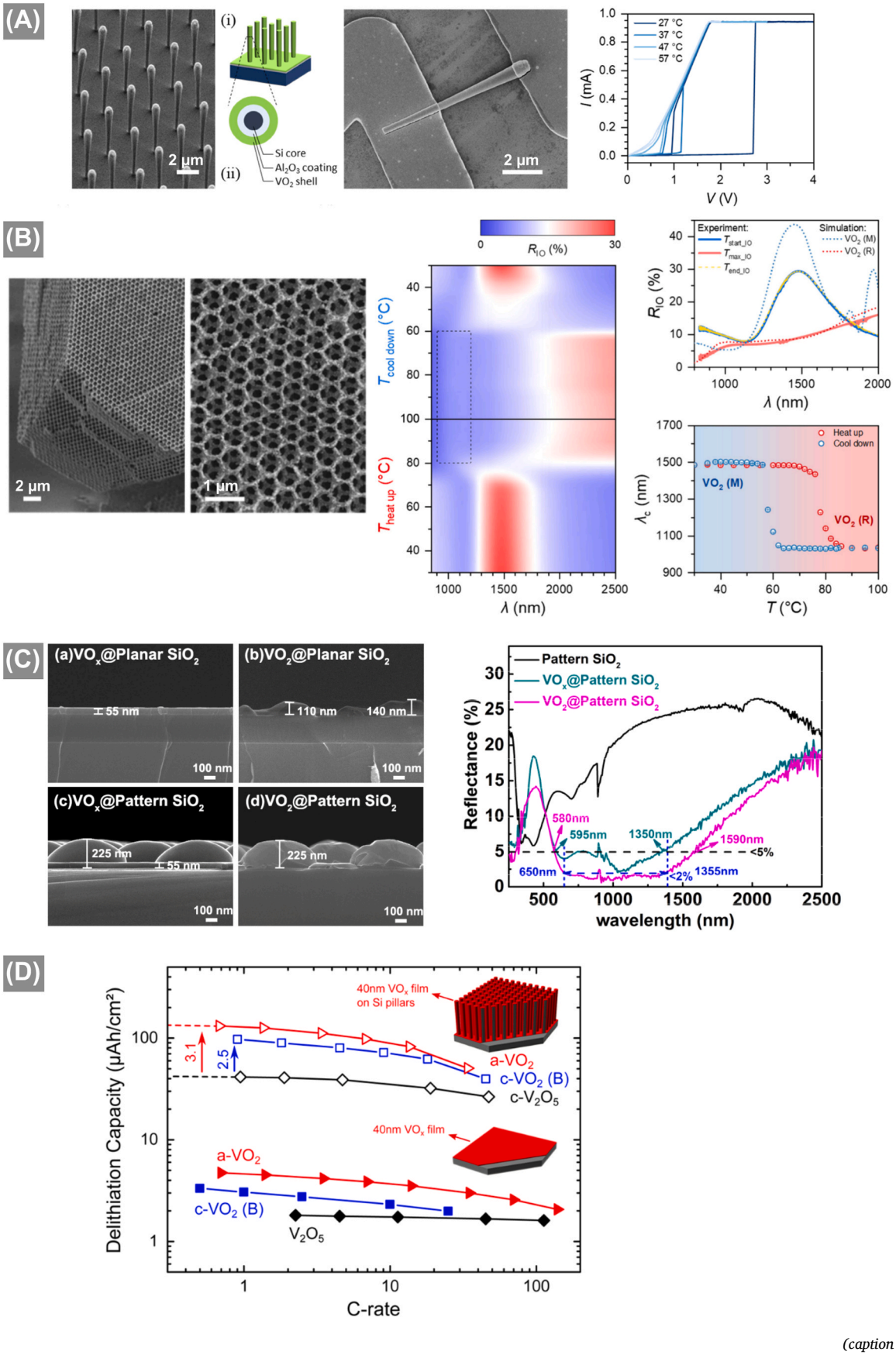

(caption on next page)

Fig. 8. ALD-based VO_2 nanostructures applied as switchable structures, antireflective materials, and in lithium ion batteries. (A) The voltage-induced switching of Si-Al_2O_3-VO_2 core-shell nanowires as 3D memristors is sensitive to the operating temperature [79]. Copyright 2025 The Authors, published by Wiley-VCH, licensed under CC-BY 4.0. (B) VO_2 inverse opal photonic crystals present reversible switching of their optical properties when the structures are heated above the IMT and cooled down [39]. Copyright 2024 The Authors, published by American Chemical Society, licensed under CC-BY 4.0. (C) Vanadium oxide coatings on patterned SiO_2 reduce the reflectance of the structures. VO_2 obtained by post-deposition annealing of the as-grown films further improves the antireflective properties [80]. Copyright 2023 The Authors, published by MDPI, licensed under CC-BY 4.0. (D) Enhanced capacity of vanadium oxide coated Si pillars compared to planar counterparts. Amorphous VO_2 coatings result in higher performances than crystalline VO_2 and V_2O_5 coatings. Figure reprinted with permission [42]. Copyright 2017, American Chemical Society.

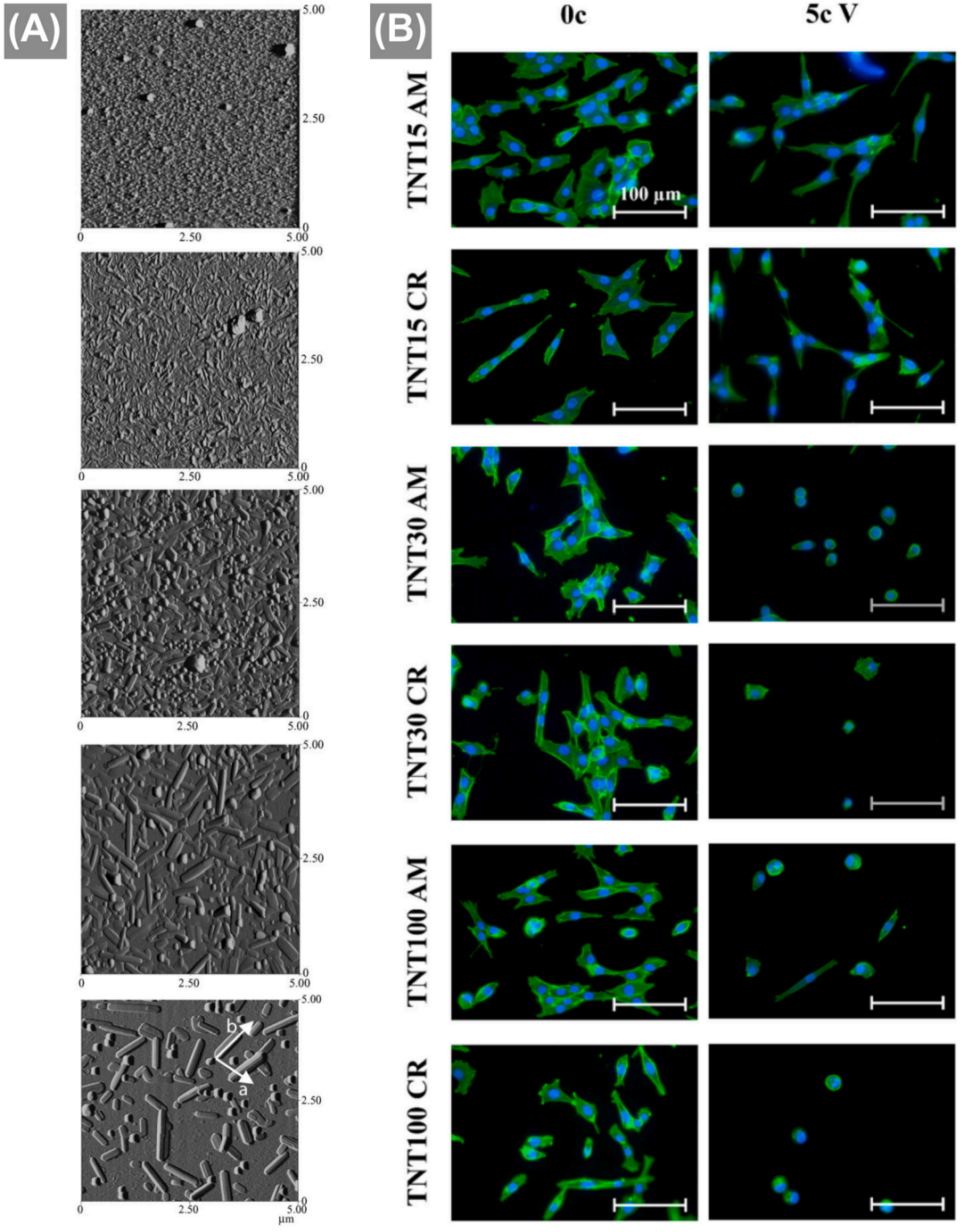

Fig. 9. (A) V_2O_5 NPs formed by annealing 5 nm thin films at 250 °C, 400 °C, 450 °C, 500 °C, and 600 °C (top to bottom). Figure adapted with permission [63]. Copyright 2006, Elsevier. (B) Influence of V_2O_5 coating (0 ALD cycles or 5 ALD cycles) and TNT templates on cell growth at the structures [81]. Copyright 2025 The Authors, published by American Chemical Society, licensed under CC-BY 4.0.

V_2O_5 batteries. The performance characteristics are summarized in Table 2, although it should be noted that the maximum capacity values are only comparable to a limited extent due to different measurement techniques. The structures on planar Si substrate utilized $VO(thd)_2$ as

Table 2
Overview of V_2O_5 nanostructures applied as battery electrodes.

Template	Intercalating species	(optimal) V_2O_5 thickness	Crystallinity	Maximum capacity	Cycling stability	Ref.
Planar Si	Li	10 nm	Crystalline	395 W/g at 960 C and 141 A/g	80% after 1530 cycles, 30% after 4000 cycles	[56]
TMV	Li	60 nm	Crystalline	25 μAh/cm^2 at 5 μAh/cm^2	98% after 50 cycles (30 nm coating)	[59]
CNTs	K	19 nm	Amorphous	191 mAh/g at 5 mA/g	≈ 80% after 50 cycles	[61]
CNTs	Li	16 nm	Amorphous	818 μA/cm^2 at 1 C	≈ 90% after 100 cycles	[70]
CNTs	Li	10 nm + 20 TiO_2 ALD cycles	Amorphous	400 mAh/g at 100 mA/g	≈ 80% after 100 cycles	[60]
CNTs	Li	≈ 15 nm + 25 TiO_2 ALD cycles	Amorphous	≈ 460 μAh at 1 C	99.6% after 100 cycles	[53]
CNTs	Li	5.5 nm	Crystalline	1209 mAh/g at 1675 mA/g	87% after 100 cycles, 73% after 450 cycles	[71]

vanadium precursor in the ALD process which resulted in rough films consisting of plate-like V_2O_5 nanocrystallites instead of conformal thin films. Although the deposition process was denoted as ALD in the publication, it comprises a CVD component evidenced by the non-conformal coating of the substrate. Nevertheless, the crystallite size was controlled by the number of cycles. Such nanostructured electrodes showed V_2O_5 thickness dependent properties in a Li-containing electrolyte. The thinner layers fabricated with 500 ALD cycles featured lower overpotential for Li^+ intercalation and deintercalation than thicker layers. Moreover, the capacity retention at higher current rates (up to 10 C) was superior for the thinner films due to an increased Li^+ intercalation based on the low thickness of these plates along their *c*-direction and corresponding short Li^+ intercalation paths. Furthermore, the structures exhibited a high cycling stability with stable capacity for 650 cycles, and a decrease to 80% and 30% of their initial performance after 1530 and 4000 cycles, respectively. Conversely, Pomerantseva *et al.* demonstrated the utilization of TMV as a biological template for V_2O_5 electrodes in 2012 [59]. A nickel layer as current collector was electrodeposited onto the self-assembled TMV structures prior to the V_2O_5 ALD coating. The O_3-based ALD process resulted in crystalline V_2O_5 without the need for an additional post-deposition annealing step. Composite electrodes with 30 nm V_2O_5 thickness showed high specific capacities of 12 μAh/cm^2 for 5 μAh/cm^2 current density and high cycling stabilities over 50 cycles for application in LIBs that were much higher than for their planar counterparts (Fig. 10A). Further, the specific capacity could be increased to 25 μAh/cm^2 by increasing the V_2O_5 thickness to 60 nm.

Still on batteries-related applications, Carter *et al.* reported disulfide shuttling in lithium-sulfur battery cathodes by utilizing V_2O_5-coated CNTs that were filled with polysulfide [71]. V_2O_5 was chosen as anchoring layer for the disulfide species based on its high polar binding to lithium polysulfides without restricting charge transfer in lithium-sulfur batteries. The performance depended on the V_2O_5 thickness with 75 V_2O_5 ALD cycles leading to the highest initial capacity of 1209 mA h/g and less decay over 50 charge/discharge cycles than for the other investigated V_2O_5 thicknesses (Fig. 10B). Although 75 ALD cycles were not sufficient in this report to entirely coat the CNTs, the incomplete coating was beneficial for charge transfer enabled polysulfide conversion which was crucial for the battery performance.

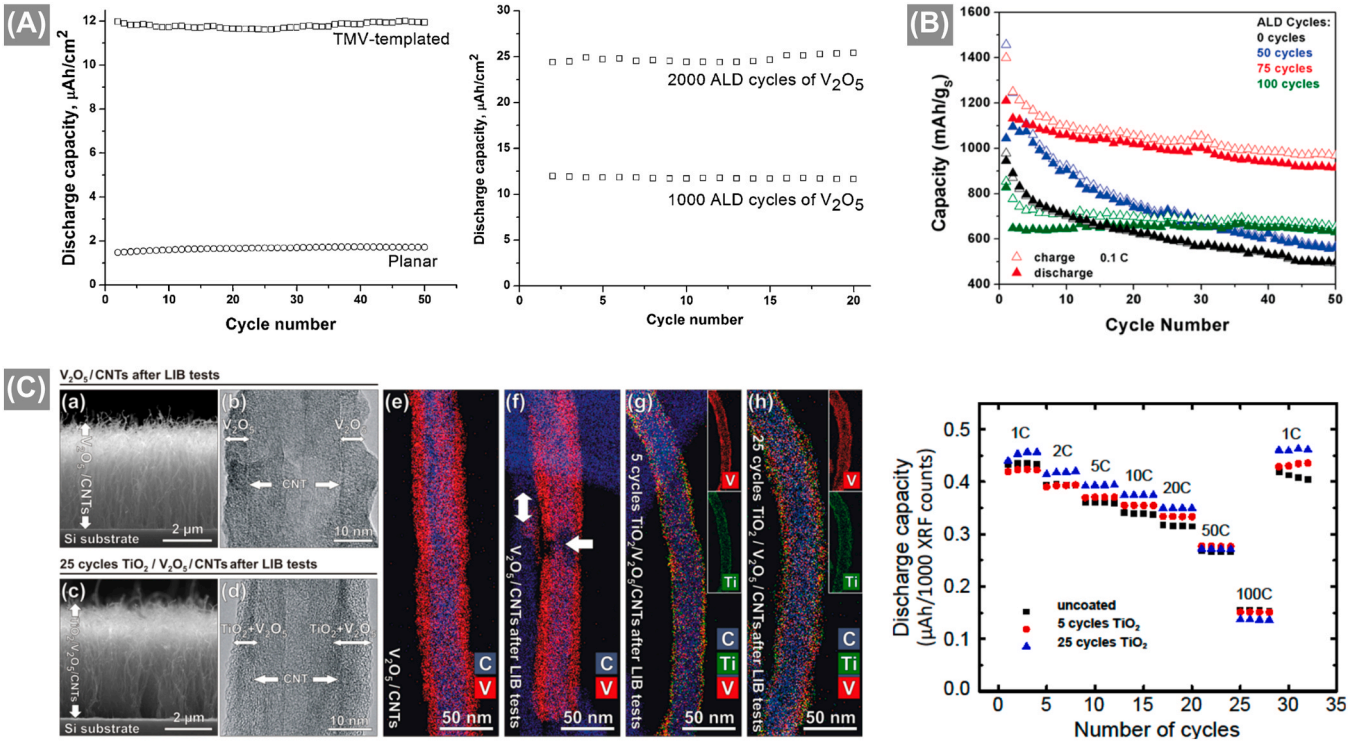

Fig. 10. V_2O_5 nanostructures applied battery electrodes. (A) Structure and thickness-dependent capacities of V_2O_5-coated tobacco mosaic virus (TMV) and planar electrodes in lithium ion batteries. Figures reprinted with permission [82]. Copyright 2012, Elsevier. (B) The capacity of V_2O_5-CNTs in lithium-sulfur batteries is highly dependent on the V_2O_5 thickness with an optimum of 75 V_2O_5 ALD cycles for a thermal ALD process using VTOP and H_2O at 150 °C deposition temperature. Figure reprinted with permission [71]. Copyright 2017, American Chemical Society. (C) Decreasing performance over repeated charging/discharging cycles is prevented by protecting V_2O_5/CNT structures with TiO_2 ALD. The performance depends on the TiO_2 thickness, the ALD cycles conditions, and the CNT template characteristics as revealed by different optimum number of applied TiO_2 ALD cycles of 25 cycles. Figure reprinted with permission [53]. Copyright 2017, American Chemical Society.

For application of a CNT/V_2O_5 composite as electrode for a potassium ion battery, amorphous V_2O_5 demonstrated a higher capacity than crystalline V_2O_5 from literature, which was associated to faster K^+ ion intercalation and deintercalation in the amorphous material [61]. Usage of CNTs as nanostructured template also led to improved Li storage capability and cycling stability compared to planar structures due to the higher surface area [70]. Although the stability of V_2O_5/CNT electrodes was higher than that of planar V_2O_5 electrodes, the capacity decreased with increasing charge-discharge cycles due to destruction of the V_2O_5 film by leaching of vanadium atoms into the electrolyte [60]. Overcoating the structure with a thin TiO_2 layer by ALD effectively prevented such decreasing capacity [53,60]. In this context, Xie *et al.* reported the highest discharge capacity of 400 mA h/g at 100 mA/g for V_2O_5/CNTs protected by 15 TiO_2 ALD cycles [60]. Nevertheless, the highest stability of the composite was observed when 20 TiO_2 ALD cycles were applied. Notably, the sequence of binder-free CNT electrode fabrication, V_2O_5 ALD, and TiO_2 ALD coating was crucial for the obtained performances. Higher capacity and rate retention were observed for first preparing the CNT electrode and subsequent functionalization with V_2O_5 and TiO_2 which was related to the electric contacts between individual CNTs. Likewise, Kurttepeli *et al.* also investigated the effect of ALD-deposited TiO_2 protective layers on the performance and structural integrity of V_2O_5/CNT electrodes in LIBs [53]. HRTEM characterization revealed that the V_xO_y ALD coating was not always completely conformal and some spots remained uncoated. For the TiO_2-coated structures, HRTEM and STEM-EDX visualization showed the layered CNT, V_2O_5, TiO_2 sequence from the CNT towards the outside (Fig. 10C), where TiO_2 coatings with 5 or 25 ALD cycles improved the Li intercalation and deintercalation kinetics up to medium C-rates of 50 C while the kinetics for 100 C were slowed down by the TiO_2 coatings. However, 25 ALD cycles TiO_2 coating could significantly stabilize the discharge capacity over 100 cycles. The unprotected V_2O_5/CNT composite lost 17% of its initial capacity after 100 cycles. A 5 TiO_2 ALD cycle protection layer reduced this loss but could not completely avoid it. In contrast, the 25

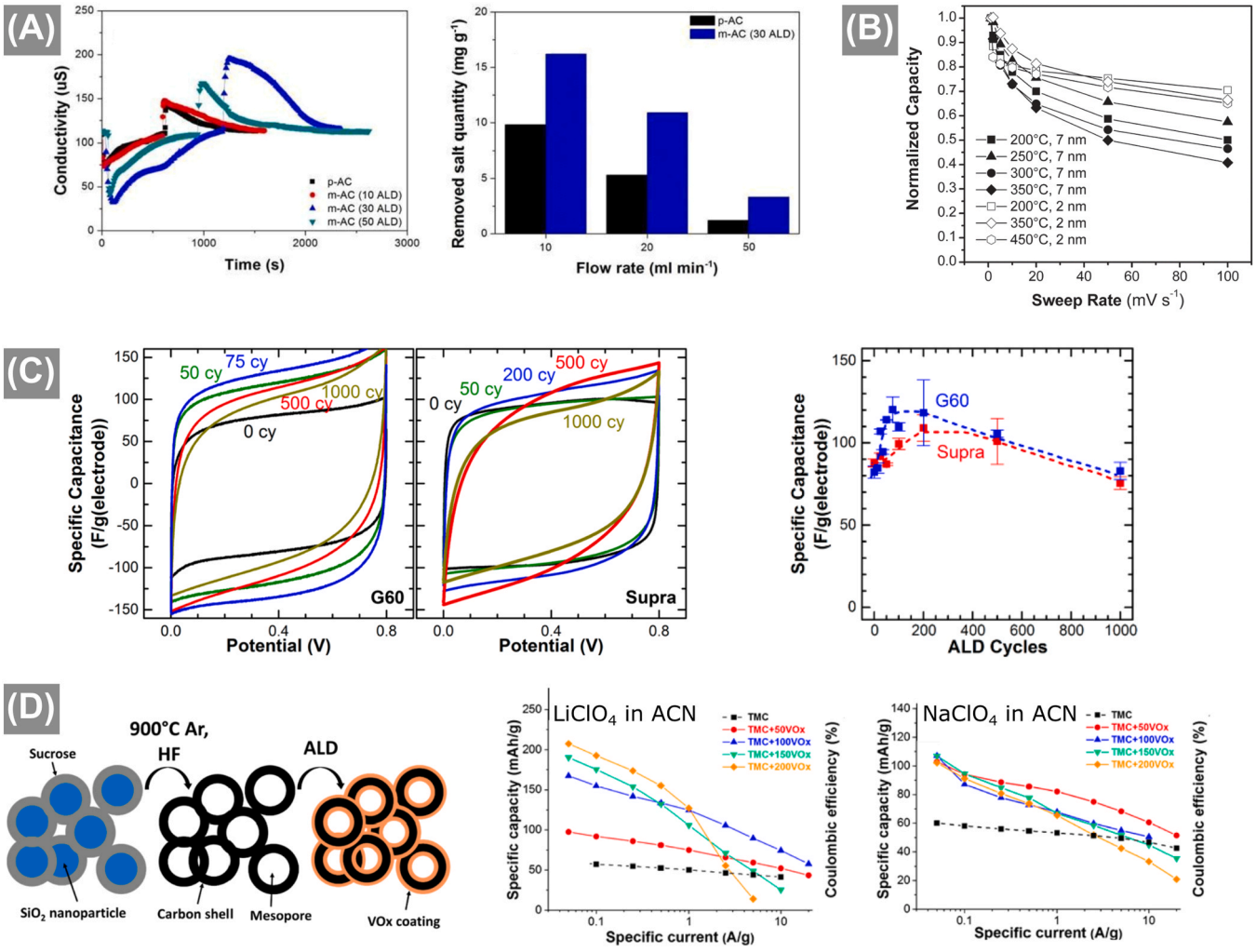

Fig. 11. Capacitor and supercapacitor applications of ALD-based V_2O_5 nanostructures. (A) Capacitive deionization of NaCl solution by pristine and modified, i.e., V_2O_5-coated active carbon (p-AC and m-AC, respectively) depends on the number of applied ALD cycles and on the flow rate of the NaCl solution. Figures adapted with permission [65]. Copyright 2022, The Korean Society of Industrial and Engineering Chemistry. (B) The normalized capacity versus the cyclic voltammetry sweep rate of V_2O_5-functionalized porous ITO electrodes is determined by the combination of V_2O_5 film thickness and the post-deposition annealing temperature. The thicker films experience grain growth and microstructure loss accompanied by decreasing capacities. Figure reprinted with permission [64]. Copyright 2014, Wiley-VCH. (C) The charge storage capacitance of V_2O_5 ALD-coated activated carbon electrodes is determined by the pore sizes. Mesoporous carbon electrodes (G60) exhibit the highest performance when functionalized with 75 V_2O_5 ALD cycles while less influence of the V_2O_5 coating thickness is obtained for microporous carbon electrodes (Supra). In the latter case, the small micropores are blocked by the vanadium precursor, hence reducing the electrodes' active surface area and decreasing the effect of the additional V_2O_5 coating. Figures adapted with permission [67]. Copyright 2015, American Chemical Society. (D) Tailored mesoporous carbon (TMC) coated with V_2O_5 is applied as Li and Na intercalating supercapacitor electrodes and presents V_2O_5 coating thickness-dependent performances. Figures adapted with permission [69]. Copyright 2017, American Chemical Society.

ALD cycles TiO_2 coating resulted in a capacity increase by ≈ 9% based on less Li accumulation, kinetically faster deintercalation, and a phase change from crystalline to amorphous V_2O_5 during charge/discharge cycles.

An all-in-one nanopore battery array based on V_2O_5-coated AAO was fabricated by Liu *et al.* in 2014 [58]. After characterizing the highly reversible Li intercalation and deintercalation in the half-cells individually, the full cell device also demonstrated high reversibility in combination with significantly higher capacity, power density, and cycling stability than earlier AAO-based full batteries. In detail, the V_2O_5/AAO battery exhibited 80 mAh/g at 150 C, about 50% capacity retention at 150 C rate, and over 80% initial capacity after 1000 charge/discharge cycles. A follow-up study by Liu *et al.* published in 2017 reported on the utilization of an asymmetric V_2O_5-SnO_2 nanopore battery where the prelithiated vanadium oxide anode was replaced with prelithiated SnO_2 and platinum was used as current collector instead of ruthenium in the earlier publication [57]. This asymmetric cell design improved the battery characteristics to 73% capacity retention at 200 C rate, 98% initial capacity after 550 charge/discharge cycles, 80% capacity after 1000 cycles, and about 100 mAh/g at 150 C.

Application of ALD-based nanostructured V_2O_5 as capacitors was highly dependent on the V_2O_5 thickness as observed by Chung *et al.* [65]. Coating V_2O_5 onto activated carbon electrodes could significantly improve the ion removal in capacitive deionization (CDI) due to the increased hydrophilicity and specific capacitance. The authors further reported thickness-dependent NaCl CDI properties with an optimum at 30 V_2O_5 ALD cycles corresponding to approximately 3.9 nm (Fig. 11A).

Besides capacitor applications, V_2O_5 nanostructures were also utilized as electrodes in supercapacitors [46,64,67–69,74]. Rauda *et al.* coated mesoporous ITO nanocrystal films with V_2O_5 thicknesses between 2 and 7 nm and both, H_2O or O_3, were used as oxygen precursors in combination with VTOP as V precursor [64]. Grain growth and loss of the microstructure occurred for 7 nm film thicknesses resulting in a normalized capacity decrease as depicted in Fig. 11B. The structure coated with 2 V_2O_5 featured higher total charge storage of 1700 C/g and capacitive charge storage of 1200 C/g than the 7 V_2O_5 composite. Moreover, it was shown that the capacitive contribution to the charge storage decreased with increasing film thickness due to the increasing diffusion control. Further, it is important to note that O_3-based V_2O_5 films exhibited higher charge storage than H_2O-based layers. The highest capacity was obtained for films annealed at 200 °C and the capacity decreased with increasing annealing duration due to grain growth and pore blocking.

Pore blocking was also reported as performance limiting issue by Daubert *et al.* for functionalizing activated carbon structures with different pore sizes [67,68]. In 2015, they reported about V_2O_5 thickness-dependent supercapacitor performance of different porous activated carbon electrodes [67]. The specific capacitance for Li intercalation increased with increasing film thickness up to a maximum value and decreased for thicker films (Fig. 11C). The highest performances were achieved with 75 ALD cycles and 200 ALD V_2O_5 cycles for the mesoporous electrode (G60) and the microporous electrode (Supra), respectively. Nevertheless, the capacity improvement was much stronger for the mesoporous sample because micropores were easily blocked by the VTOP precursor resulting in a decreased surface area of the electrode. The stability over 10000 charge/discharge cycles was similar to uncoated structures for both electrodes. In a subsequent study, simulations confirmed that coating of pores with diameters below 1.3 nm resulted in too small open volume for reactant diffusion [68]. V_2O_5-coated activated carbon electrodes demonstrated increased pseudocapacitive energy storage compared to uncoated electrodes whereby the V_2O_5 thickness and pore size determined the performance as depicted in Fig. 11C. While microporous and mesoporous samples showed only a slight capacity increase due to diffusion limitation, both macroporous carbon samples exhibited significant capacity improvement up to 83%. However, charge storage in the microporous carbon black sample changed to battery-like behavior with increasing V_2O_5 thickness in contrast to the capacitive behavior of the activated carbon samples. Similarly, mesoporous carbon was also applied as template for V_2O_5 PEALD coating by Fleischmann *et al.* for application in Li and Na intercalating supercapacitor electrodes [69]. V_2O_5 coating increased the capacity for Li intercalation from 60 mAh/g of the uncoated structure to 210 mAh/g with 200 V_2O_5 PEALD cycles as depicted in Fig. 11D. Nevertheless, the high thickness led to significant capacity decay at high C rates and the thickness increase was accompanied by a change to diffusion-limited battery-like charge storage. Thus, a medium coating thickness of 100 PEALD cycles resulting in a maximum capacity of 170 mAh/g was chosen to balance both effects. In contrast, the V_2O_5 loading had only a minor effect on the capacity when the electrodes were applied in Na electrolytes as a new route for V_2O_5 batteries. Na ions could not diffuse through the entire V_2O_5 layers due to the larger ionic radius. Hence, intercalation occurred in the vicinity of the surface and accordingly, increasing the V_2O_5 thickness did not benefit the performance. Notably, Li intercalation was characterized by a mixture of pseudocapacitive and battery-like behavior while Na intercalation was almost completely pseudocapacitive. The structures also presented a high long-term stability with 116% and 75% of the initial capacities after 2000 charge/discharge cycles in Li and Na electrolytes, respectively. The combination of nanometer-thin V_2O_5 layers and their confinement in the mesopores enabled the application as Na electrolyte supercapacitor with the highest stability reported for a V_2O_5-based structure until the publishing date of the study in 2017. Lee *et al.* reported on another carbon/V_2O_5 composite electrode by utilizing multilayer graphene as template for the ALD coating [74]. Amorphous V_2O_5 resulted in a higher capacity, energy density, and stability than the crystalline structure due to improved Li intercalation.

3.4. V_xO_y (Mixed valance)

Application of ALD-based V_xO_y nanostructures consisting of mixed valance state was reported for the fields of energy storage [21,28,30,46] and catalysis [22,23,25,26,27,29,31]. Düngen *et al.* characterized and optimized the influence of ALD parameters on the morphology and composition of V_xO_y-deposition on CNTs [32]. Although only one ALD cycle was applied, they revealed that a pretreatment of the CNTs prior to the ALD coating had a significant effect on the ALD process by creating functional groups at the CNT surface. Among anhydride and phenol groups, carboxylic groups were beneficial for the reaction with VTOP as examined by DFT calculations of VTOP reacting with different functional groups. The ALD process was optimized based on the maximal carboxylic acid consumption per ALD parameter to obtain the highest amount of V_xO_y chemically bound to the CNTs. In detail, the VTOP pulse time, purging duration between the pulses, and the deposition temperature were studied.

Utilization of only a few ALD cycles was frequently reported for catalytic applications. Keränen *et al.* observed in two studies an improved dispersion of ALD-deposited V_xO_y clusters on Al_2O_3, SiO_2, or TiO_2 particle powders as support material compared to clusters fabricated by wet impregnation [22,26]. Moreover, they detected an increased acidity and bonding strength of the structures leading to a higher ammonia uptake. Furthermore, the catalytic activity for oxidative propane dehydrogenation increased by a factor of 1.6–1.8 compared to the wet impregnated structures [22]. As in the previous example, ALD-based V_xO_y nanostructures were applied as catalysts for oxidative dehydrogenation of different compounds, namely ethanol [23], cyclohexane [25], and ethylbenzene [31]. For instance, Yang *et al.* functionalized Al_2O_3 powder with one to twelve V_xO_y ALD cycles whereby the V_xO_y phase changed with increasing cycle number from monomeric V_xO_y to polymeric V_xO_y and crystalline V_2O_5 (> 8 ALD cycles) as schematically depicted in Fig. 12A [31]. For the catalysis tests, the monomeric V_xO_y prepared by one ALD cycle presented the highest stability and featured the highest activity due to the Al-O-V bond. Similar

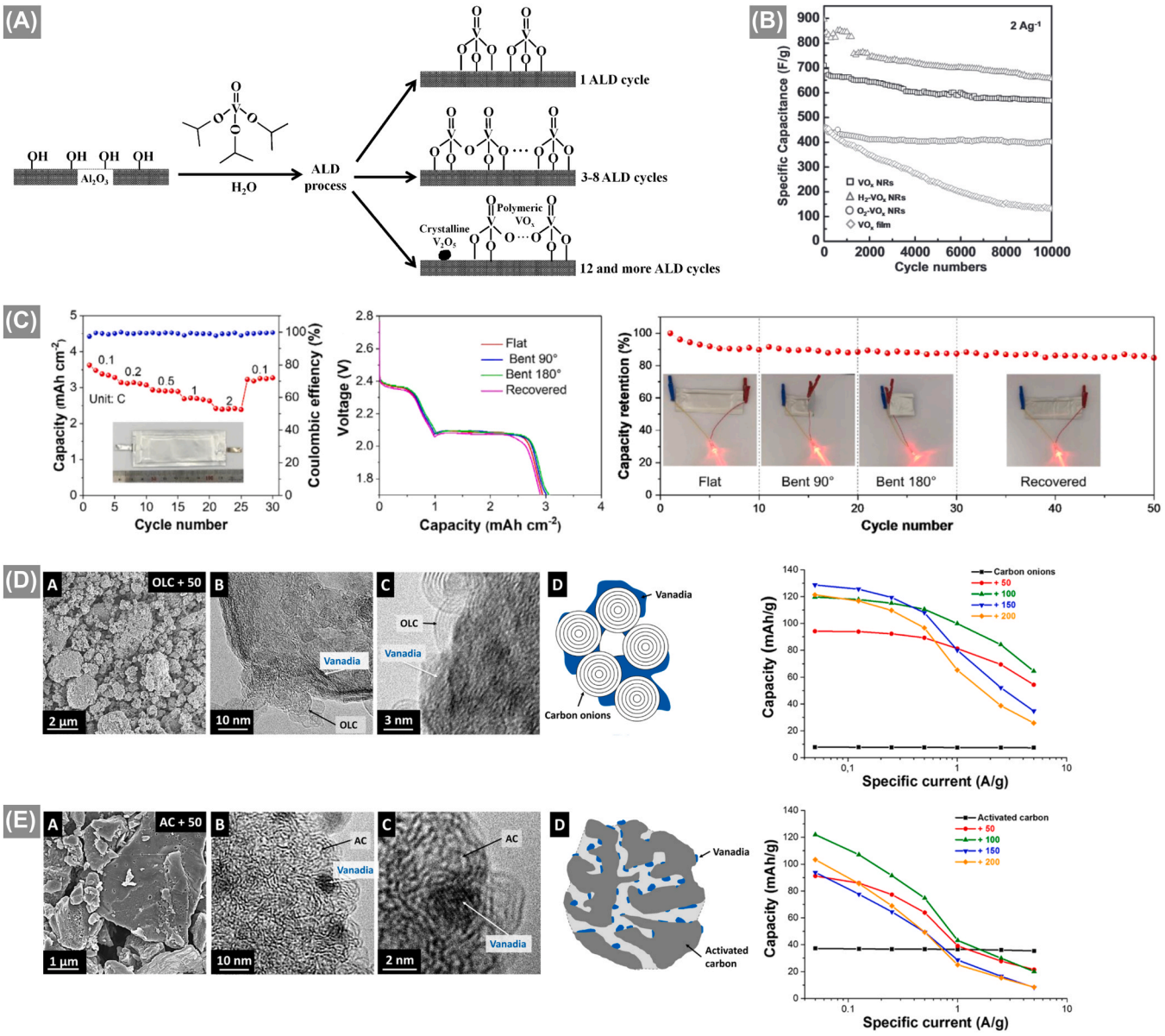

Fig. 12. Application of ALD-based V_xO_y nanostructures. (A) Schematic of V_xO_y ALD on a substrate surface depicting the formation of monomeric and polymeric V_xO_y species due to the different V_xO_y ALD cycle numbers. Figure reprinted with permission [31]. Copyright 2019, Elsevier. (B) Li storage capacitance of ALD-grown V_xO_y nanorods (NRs) branching from SiNWs over multiple charging/discharging cycles. The initial performance and the decay over charging/discharging cycles depend strongly on the post-deposition annealing atmosphere (without, H_2, or O_2). Figure reprinted with permission [46]. Copyright 2017, Wiley-VCH. (C) Characteristics and application tests of a VC/V_2O_3 hybrid structure as flexible Li-S battery during bending to different angles. Figures reprinted with permission [35]. Copyright 2022, Elsevier. (D-E) SEM and TEM images, schemes, and Li storage capacities of (D) onion-like carbon (OLC) and (E) activated carbon (AC) structures coated with V_xO_y. The applied number of V_xO_y ALD cycles defines their structure and electrochemical energy storage behavior. Figures reprinted with permission [28]. Copyright 2016, American Chemical Society.

results of few ALD cycles V_xO_y-coated Al_2O_3 powder were obtained by Wu *et al.* who investigated the methanol oxidation to formate [29]. Furthermore, embedding V_xO_y clusters fabricated by one ALD cycle in Al_2O_3, SiO_2, or TiO_2 as support material resulted in increased V_xO_y loadings and dispersion compared to conventionally supported clusters [23]. The V_xO_y ALD was conducted on a graphene oxide template that was removed after the embedding material, i.e., the catalyst support material, was deposited by ALD. Graphene oxide template removal was either conducted by calcination in air at 550 °C for 6.5 h or by treatment in O_3 at 150 °C for 10 days. Interestingly, calcined samples exhibited higher selectivity in the catalytic oxidative ethanol dehydrogenation while samples treated in O_3 showed higher activity. Raman measurements revealed that the support material determined the phase of the V_xO_y clusters. In detail, amorphous V_xO_y was observed for Al_2O_3 and TiO_2 supports and crystalline V_2O_5 formed in SiO_2 support. The combination of ALD-deposited V_xO_y and TiO_2 films on mesoporous silica (SBA−15) and mesoporous phenol/formaldehyde resin (FDU−15) supports as catalysts for cyclohexene epoxidation was additionally studied by Muylaert *et al.* in 2012 [27]. The selectivity for epoxidation in the catalytic reaction increased with increasing V_xO_y ALD cycles for SBA−15 support. Contrary, the V_xO_y on FDU−15 support was not catalytically active for the cyclohexene epoxidation. Mixed layers of TiO_2 and V_xO_y could significantly improve the selectivity towards the epoxidation for SBA−15 support.

Supercapacitor applications were tested with V_xO_y ALD-coated CNTs [30], Si NW [46], and graphene fibers [21]. The CNT-based electrodes

exhibited higher capacitance than commercially available activated carbon electrodes at the time of publication in 2012 [30]. ALD coating with 100 V_xO_y cycles resulted in the highest capacitance of 1550 F/g at 1 A/g which decreased with increasing ALD cycle numbers due to the prolonged Li diffusion paths in the V_xO_y layers. Besides V_xO_y on CNTs, ALD-grown V_xO_y nanorods (NRs) that branched from Si NWs exhibited more stable supercapacitor performance for mixed V_xO_y phase than for pure V_2O_5 or VO_2 over 10000 charge/discharge cycles [46]. Crystalline V_2O_5 and VO_2 NRs were obtained by annealing the structures in O_2 and H_2, respectively. The H_2-treated sample showed the highest specific capacitance for Li storage of 930 F/g at 1 mV/s scan rate. Although the O_2-treated sample provided the highest stability of 91.1% after 10000 charge/discharge cycles, the capacity of the as-prepared structure was significantly higher but a lower stability of 81.3% was observed (Fig. 12B). Hence, the V_xO_y NR structure could be easily tailored for the desired properties, e.g., specific capacity or stability, by adapting the post-deposition annealing process. Furthermore, Deshmukh *et al.* demonstrated the fabrication of a binder-free flexible gel supercapacitor electrode by depositing V_xO_y onto laser-induced graphene fibers [21]. The area capacity could be significantly improved compared to the uncoated fibers. Specifically, the electrodes featured capacities of 99 mF/cm^2 at 1 mA/cm^2 in an aqueous electrolyte and 2 mF/cm^2 at 0.25 mA/cm^2 in a gel electrolyte. Further, a stable capacitance of 93% of the initial value was obtained after 11500 charge/discharge cycles. The charge storage process was mostly capacitive-controlled but the influence of diffusion-limitation was also observed. The latter one decreased with increasing sweep rate. A solid-state flexible gel supercapacitor showed high long-term stability upon bending independent of the bending degree.

Energy storage applications of nanostructures based on ALD-deposited V_xO_y and other stoichiometric vanadium oxides than previously discussed included batteries [28,34,35] and supercapacitors [21, 28,30,46]. Nguyen *et al.* fabricated VC/V_2O_3 hybrid structures by ALD-coating V_xO_y on porous carbon textile templates followed by post-deposition annealing in air at 900 °C for 1 min [35]. For application in Li-S batteries, they could suppress Li dendrite formation in the anode resulting in a high capacity of 882 mAh/g at 5 C and a very high stability of 99.98% after 1000 charge/discharge cycles at 1 C. The good performance was based on polysulfide trapping by defective V_2O_3 in combination with increased polysulfide fragmentation by the conductive VC part. Furthermore, the utilization in flexible Li-S batteries was demonstrated over multiple cycles and under different bending angles as shown in Fig. 12C. Later in 2022, the same group applied defective hydrated V_xO_y-coated porous carbon textile structures as electrodes in Zn ion batteries (ZIBs) [34]. VOH was formed from the previously reported structures after storage in ambient air and at room temperature for 30 days. The defective nature of VOH was crucial for the ZIB performance since it enhanced Zn^{2+} adsorption and intercalation into the electrode structures. Thus, an increase of the capacity from 352 mAh/g to 416 mAh/g was observed for the change from defect-free VOH to defective VOH. Moreover, the defective VOH structure retained 85.8% of its initial capacity after 1000 charge/discharge cycles at 1 A/g and 88% after 2000 cycles at 5 A/g. A flexible ZIB displayed stable performance over 50 folding/unfolding cycles.

In 2016, Fleischmann *et al.* explored the fundamental properties of V_xO_y-functionalized endo- and exohedral carbon in lithium-based energy storage [28]. V_xO_y coating was present on the inside and outside of onion-like carbon (OLC) agglomerates as an exohedral template (Fig. 12D). Porous activated carbon (AC) represented an endohedral template and was mostly coated within the pores as shown in Fig. 12E. Raman spectra revealed that the V_xO_y coating on OCL templates consists of a mixture of crystalline V_2O_3, VO_2, and V_2O_5 domains while a coated AC template shows mostly amorphous regions with small crystalline V_2O_5 areas. The template type and V_xO_y coating thickness determined the capacitive behavior of the structures. For OCL structures, capacitive Li storage was observed for uncoated templates. The specific current of V_xO_y coated OLC templates increased significantly with increasing V_xO_y ALD cycle numbers (Fig. 12D) due to a change to battery-like behavior. The strongest current peaks were observed for 50 V_xO_y ALD cycles and corresponded to a fast Li intercalation. Slower intercalation occurred for thicker coatings. However, the capacity of the structures increased up to 100 or 150 ALD cycles for high and low specific currents. Coating AC templates with V_xO_y also improved their Li storage capacity compared to the uncoated counterparts. In contrast to the OLC structures, all AC structures presented capacitive charge storage behavior. The highest performance was obtained with 100 V_xO_y ALD cycles and it declined significantly for thicker films caused by the increased Li diffusion paths in the material. In general, the AC structures performed worse than the OLC structures for two reasons: first, the electrical conductivity of AC is approximately one order of magnitude smaller than that of OLC which limits the performance at high scan rates. Second, the small internal pores in the AC structures were blocked by coatings above 100 ALD cycles whereby the available surface area reduced. Nevertheless, both template types showed good stability of 95% after 3000 charge/discharge cycles applied to the individual half-cells.

4. Challenges and future perspectives

The reviewed literature on V_xO_y nanostructures demonstrates that ALD of vanadium oxides offers a variety of options with respect to both, vanadium and oxygen precursors, to ALD modes, deposition temperature, and further process conditions. Several publications have shown that the vanadium precursors and especially the vanadium oxidation state within the precursor compound is determinant for the phase of the ALD-deposited V_xO_y. Similar to planar thin films, post-deposition annealing is often applied to crystallize the as-deposited V_xO_y nanostructures into a certain desired phase. Nevertheless, ALD coating of nanostructured templates goes along with a plethora of substrates which can also influence the V_xO_y crystallization behavior and properties. Hence, the control of the vanadium oxides' phases in nanostructures remains quite challenging and requires precise adjustment and optimization of the applied process conditions – both during ALD and post-deposition annealing. It is worth emphasizing that the multiple fabrication steps generate a complex parameter space as visualized in Fig. 13. Interdependencies in this parameter space are difficult to predict due to the complexity. Hence, AI-assisted process optimization might be helpful in the future for obtaining V_xO_y nanostructures with certain desired properties.

On the other hand, the wide range of available process parameters (see overview in Table 1) allows for utilizing different ALD process to fabricate ALD-based V_xO_y nanostructures. For example, the V_xO_y phase on a nanostructured substrate could be easily tuned for the desired

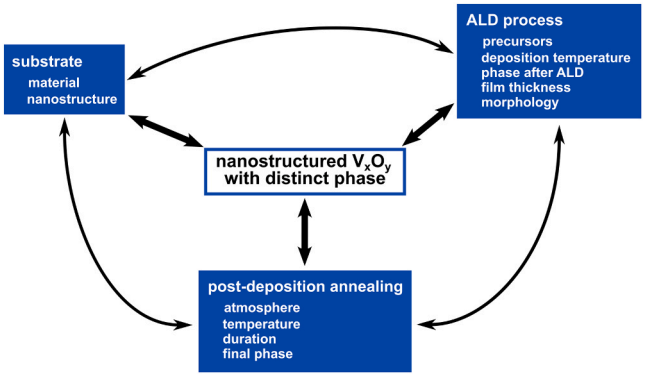

Fig. 13. Schematic illustrating the dependencies between an utilized substrate, the ALD process, and applied post-deposition annealing conditions to obtain ALD-based nanostructured V_xO_y with distinct phases. Each of the processing steps requires several parameters which leads to complex interdependencies.

application by adjusting the post-deposition annealing conditions – especially the atmosphere – without the need of establishing a completely new ALD process fabrication route. Moreover, the ALD process can be chosen to align with inherent limitations from the substrate such as temperature stability for polymeric structures. Owing to this flexibility in ALD-based V_xO_y nanostructure fabrication, applications of different nanostructured V_xO_y phases have been demonstrated in various fields, namely catalysis, energy storage, optics, sensing, and stimuli-induced properties switching. The improved functional properties of nanostructured V_xO_y could be extended to different templates – both regarding their geometrical nanostructure and the template material – to generate new or expand the existing functionalities. However, it has to be noted that such transfer could potentially require a modification of the post-processing conditions. If processing parameters for fabricating new structures only need to be slightly modified or are obtained fast, this generates high potential for applications of the structures. On the other hand, the parameter space complexity might prolong a necessary process optimization with regard to specific properties which would limit the range of suitable modifications for potential applications.

ALD not only enables conformal coating of complex 3D substrates, but also allows to accurately control the deposited film thickness on a sub-nm scale. Hence, it facilitated thickness-dependent studies of the V_xO_y nanostructures' properties in the aforementioned application fields. For example, V_2O_5 batteries presented different optimal V_xO_y film thicknesses depending on the nanostructure template, the battery type, and the operating conditions. Optimization of the film thickness in various applications for maximizing the performance could further reduce the material consumption by the need of less material. This renders the structures and devices not only less costly but also more sustainable. If multiple process step modifications are necessary, the large parameter space might require several optimization loops before the desired sample is obtained as previously discussed. The fact that amorphous V_xO_y structures present often better energy storage characteristics than crystalline ones make ALD an excellent method for depositing V_xO_y since most ALD processes inherently lead to amorphous films.

Selected area crystallization of as-deposited V_xO_y films on nanostructured templates might be achieved by photoinduced crystallization. As it was discussed in Section 3.2, photoinduced oxidation into V_2O_5 was observed when VO_2 NPs were irradiated with a high-intensity laser beam in ambient atmosphere [48,49]. Such procedure could be useful for oxidizing only sub-regions of the V_xO_y nanostructure to generate different functional phases on the same substrate. Further, photoinduced oxidation could be an alternative to thermal annealing as post-deposition processing of the ALD-deposited V_xO_y thin films. Nevertheless, up to now this is a hypothetical approach which was reported for other materials [83–85] but necessitates further research for V_xO_y.

Deposition of only one V_xO_y ALD cycle on Al_2O_3 is often beneficial for catalytic applications because the V_xO_y is present in the monomeric phase. This component provides higher catalytic activity than polymeric V_xO_y for certain reactions due to the formation of an Al-O-V bond [31]. Hence, further research in this field may focus on the utilization of Al-based nanostructure templates for single cycle V_xO_y ALD. Alternatively, one could also combine an Al precursor with a V_xO_y ALD process in a so-called supercycle to introduce Al atoms directly in the V_xO_y coating [11,86–88]. Such supercycle ALD process offers the advantage to freely choose the nanostructure template material since the catalytically highly active Al-O-V bond will be created during the material deposition.

In addition, ALD supercycles also present an option to further tune the properties of V_xO_y nanostructures by combining V_xO_y with other materials in the form of doping or as multilayers [11,86–88]. Especially VO_2 is an interesting candidate for doping and multilayering since such approaches can tailor its IMT – potentially down to room temperature as demonstrated for planar thin films synthesized with various methods [89–98], but not yet for 3D nanostructures. The ALD-based switchable VO_2 nanostructures reviewed in this article represent promising components for smart windows based on their IMT at comparable low temperatures around 68 °C. While it was shown that the ALD-based preparation of VO_2 on nanostructured templates is less trivial than other phases, it was successfully reported in some publications utilizing different vanadium precursors and process conditions. Hence, these fabrication processes could be potentially transferred to further nanostructures to improve their stimuli-induced property switching.

A critical aspect for VO_2 nanostructures in general is the low stability for storing samples since VO_2 is not the most thermodynamically stable V_xO_y phase [2,18]. Accordingly, it tends to transform into other phases, especially V_2O_5, over longer periods when it is exposed to ambient conditions. Such undesired phase transition could be enhanced in nanostructures due to their large surface-to-volume ratio, which limits the practical applicability of VO_2 structures. An approach to prevent the phase transition is to overcoat the structure with an ultra-thin protection layer, also called encapsulation [99–104]. With ALD, protection layers can be easily deposited on the VO_2 nanostructures by applying few cycles of a more stable material – e.g., Al_2O_3, TiO_2, or ZnO serving as moisture and oxygen diffusion barrier – are commonly used due to their robustness, low precursor costs, and well-established ALD processes [99–103].

5. Conclusion

This review highlighted recent progress in ALD-based fabrication of functional vanadium oxide nanostructures for application in various fields. A summary of the applied ALD processes and post-deposition annealing conditions showed that several vanadium precursors are suitable for V_xO_y ALD on nanostructures. Further, our review demonstrated that the ALD process conditions and post-deposition annealing parameters need to be carefully chosen based on the nanostructured substrate and the desired V_xO_y phase. Especially the phase control remains challenging and requires precise optimization of the individual processing steps including multiple parameters and complex interdependencies. Nevertheless, ALD features the inherent advantages of conformal coating complex shapes – such as nanostructured substrates – combined with film thickness control in the sub-nm range. Film-thickness dependent studies have shown significant potential for optimizing performances of V_xO_y nanostructures in catalysis, sensing, energy storage, and switchable optoelectronics.

Future directions could target studies of supercycle ALD to combine V_xO_y with other materials in nanostructures in order to expand or to tailor their properties. Nevertheless, the multi-dimensional processing parameter space could impede such approaches. Moreover, our review demonstrated that phase control in nanostructures is more challenging than in planar films, so that special focus needs to be placed on the V_xO_y phase control during ALD and post-deposition annealing to ensure the fabrication of the desired phase. Application of ultra-thin ALD-grown protection layers are a promising approach to maintain the V_xO_y phase over long time. "Smart" devices which feature a property change induced by external stimuli show great potential for the future. Here, VO_2 present enormous prospects for devices such as smart windows based on the materials' inherent IMT at a relatively low temperature that leads to reversible switching of the optoelectronic properties.

In conclusion, ALD-based vanadium oxide nanostructures are a versatile material class according to the variety of V_xO_y phases. They present huge potential in the fields of catalysis, energy storage, optics, sensing, and stimuli-induced properties switching. Nevertheless, challenges in controlling the V_xO_y phase and maintaining it over a long time period still hinder their practical capabilities at the moment. Our review provides an overview of the available ALD V_xO_y processes for nanostructures and the associated challenges to generate each of the phases of interest. Future research focused on overcoming the phase control and

stability limitations might enable the expansion of the functionalities of V_xO_y nanostructures by adjusting the nanostructure geometries as well as the V_xO_y coating properties. Understanding and controlling the complex interdependencies of processing parameters presents a prerequisite to targeted sample preparation and could benefit from AI-assisted optimization approaches. Hence, ALD may provide a pathway toward the development of tailor-made, high-performance V_xO_y nanostructures for sustainable technologies in the future.

CRediT authorship contribution statement

Carina Hedrich: Writing – original draft, Visualization, Formal analysis, Conceptualization. **Robert H. Blick:** Writing – review & editing, Resources, Funding acquisition. **Martin Ritter:** Writing – review & editing, Supervision. **Robert Zierold:** Writing – review & editing, Funding acquisition. **Pagnan Furlan Kaline:** Writing – review & editing, Supervision, Resources, Project administration, Funding acquisition, Conceptualization.

Declaration of Competing Interest

The authors declare the following financial interests/personal relationships which may be considered as potential competing interests: Kaline Pagnan Furlan reports financial support was provided by German Research Foundation. If there are other authors, they declare that they have no known competing financial interests or personal relationships that could have appeared to influence the work reported in this paper.

Acknowledgements

Funded by the Deutsche Forschungsgemeinschaft (DFG, German Research Foundation) as part of the Excellence Strategy of the Federal Government and the federal states - EXC 3120/1 BlueMat: Water-Driven Materials -533771286 (PIs Pagnan Furlan, Zierold and Blick). The authors further acknowledge DFG funding via the SFB 1615 “SMART Reactors for Future Process Engineering” (project number 503850735).

Data Availability

Data will be made available on request.

References

[1] P. Hu, P. Hu, T.D. Vu, M. Li, S. Wang, Y. Ke, X. Zeng, L. Mai, Y. Long, Vanadium oxide: phase diagrams, structures, synthesis, and applications, Chem. Rev. 123 (2023) 4353–4415, https://doi.org/10.1021/acs.chemrev.2c00546.
[2] N. Bahlawane, D. Lenoble, Vanadium oxide compounds: structure, properties, and growth from the gas phase, Chem. Vap. Depos. 20 (2014) 299–311, https://doi.org/10.1002/cvde.201400057.
[3] C. Wu, H. Wei, B. Ning, Y. Xie, New vanadium oxide nanostructures: controlled synthesis and their smart electrical switching properties, Adv. Mater. 22 (2010) 1972–1976, https://doi.org/10.1002/adma.200903890.
[4] Y. Wang, G. Cao, Synthesis and enhanced intercalation properties of nanostructured vanadium oxides, Chem. Mater. 18 (2006) 2787–2804, https://doi.org/10.1021/cm052765h.
[5] C. Wu, F. Feng, Y. Xie, Design of vanadium oxide structures with controllable electrical properties for energy applications, Chem. Soc. Rev. 42 (2013) 5157–5183, https://doi.org/10.1039/C3CS35508J.
[6] C. Wu, Y. Xie, Promising vanadium oxide and hydroxide nanostructures: from energy storage to energy saving, Energy Environ. Sci. 3 (2010) 1191–1206, https://doi.org/10.1039/C0EE00026D.
[7] V.P. Prasadam, N. Bahlawane, F. Mattelaer, G. Rampelberg, C. Detavernier, L. Fang, Y. Jiang, K. Martens, I.P. Parkin, I. Papakonstantinou, Atomic layer deposition of vanadium oxides: process and application review, Mater. Today Chem. 12 (2019) 396–423, https://doi.org/10.1016/j.mtchem.2019.03.004.
[8] J. Schoiswohl, S. Surnev, F.P. Netzer, G. Kresse, Vanadium oxide nanostructures: from zero- to three-dimensional, J. Phys. Condens. Matter 18 (2006) R1, https://doi.org/10.1088/0953-8984/18/4/R01.
[9] H. Jerominek, F. Picard, D. Vincent, Vanadium oxide films for optical switching and detection, Opt. Eng. 32 (1993) 2092–2099, https://doi.org/10.1117/12.143951.
[10] S.M. George, Atomic layer deposition: an overview, Chem. Rev. 110 (2010) 111–131, https://doi.org/10.1021/cr900056b.
[11] V. Miikkulainen, M. Leskelä, M. Ritala, R.L. Puurunen, Crystallinity of inorganic films grown by atomic layer deposition: overview and general trends, J. Appl. Phys. 113 (2013), https://doi.org/10.1063/1.4757907.
[12] R.L. Puurunen, Surface chemistry of atomic layer deposition: a case study for the trimethylaluminum/water process, J. Appl. Phys. 97 (2005) 121301–121353, https://doi.org/10.1063/1.1940727.
[13] V. Cremers, R.L. Puurunen, J. Dendooven, Conformality in atomic layer deposition: Current status overview of analysis and modelling, Appl. Phys. Rev. 6 (2019) 021302, https://doi.org/10.1063/1.5060967.
[14] M. Leskelä, M. Ritala, Atomic layer deposition (ALD): from precursors to thin film structures, Thin Solid Films 409 (2002) 138–146.
[15] M. Knez, K. Nielsch, L. Niinistö, Synthesis and surface engineering of complex nanostructures by atomic layer deposition, Adv. Mater. 19 (2007) 3425–3438, https://doi.org/10.1002/adma.200700079.
[16] H. Kim, H.B.R. Lee, W.J. Maeng, Applications of atomic layer deposition to nanofabrication and emerging nanodevices, Thin Solid Films 517 (2009) 2563–2580, https://doi.org/10.1016/j.tsf.2008.09.007.
[17] C. Bae, H. Shin, K. Nielsch, Surface modification and fabrication of 3D nanostructures by atomic layer deposition, MRS Bull. 36 (2011) 887–897, https://doi.org/10.1557/mrs.2011.264.
[18] C. Lamsal, N.M. Ravindra, Optical properties of vanadium oxides-an analysis, J. Mater. Sci. 48 (2013) 6341–6351, https://doi.org/10.1007/s10853-013-7433-3.
[19] M. Kang, I. Kim, S.W. Kim, J.-W. Ryu, H.Y. Park, Metal-insulator transition without structural phase transition in V_2O_5 film, Appl. Phys. Lett. 98 (2011) 131907, https://doi.org/10.1063/1.3571557.
[20] G. Rampelberg, D. Deduytsche, B. De Schutter, P.A. Premkumar, M. Toeller, M. Schaekers, K. Martens, I. Radu, C. Detavernier, Crystallization and semiconductor-metal switching behavior of thin VO_2 layers grown by atomic layer deposition, Thin Solid Films 550 (2014) 59–64, https://doi.org/10.1016/j.tsf.2013.10.039.
[21] S. Deshmukh, W. Gao, J. Michalička, M. Pumera, Nanoscopic decoration of multivalent vanadium oxide on Laser-Induced graphene fibers via atomic layer deposition for flexible gel supercapacitors, Chem. Eng. J. 480 (2024) 147895, https://doi.org/10.1016/j.cej.2023.147895.
[22] J. Keränen, A. Auroux, S. Ek, L. Niinistö, Preparation, characterization and activity testing of vanadia catalysts deposited onto silica and alumina supports by atomic layer deposition, Appl. Catal. Gen. 228 (2002) 213–225, https://doi.org/10.1016/S0926-860X(01)00975-9.
[23] P. Ruff, L. Schumacher, S. Rogg, C. Hess, Atomic Layer Deposition-Assisted Synthesis of Embedded Vanadia Catalysts, ACS Catal. 9 (2019) 6349–6361, https://doi.org/10.1021/acscatal.9b01385.
[24] J. He, H. Song, J. Li, Z. Li, S. Liu, Continuum ALD model unlocks controllable growth of VOx nanorods in high-aspect-ratio structures at elevated temperatures, Cryst. Growth Des. 25 (2025) 8854–8862, https://doi.org/10.1021/acs.cgd.5c00436.
[25] H. Feng, J.W. Elam, J.A. Libera, M.J. Pellin, P.C. Stair, Oxidative dehydrogenation of cyclohexane over alumina-supported vanadium oxide nanoliths, J. Catal. 269 (2010) 421–431, https://doi.org/10.1016/j.jcat.2009.11.026.
[26] J. Keränen, C. Guimon, E. Iiskola, A. Auroux, L. Niinistö, Atomic layer deposition and surface characterization of highly dispersed titania/silica-supported vanadia catalysts, Catal. Today 78 (2003) 149–157, https://doi.org/10.1016/S0920-5861(02)00320-6.
[27] I. Muylaert, J. Musschoot, K. Leus, J. Dendooven, C. Detavernier, P. Van Der Voort, Atomic layer deposition of titanium and vanadium oxide on mesoporous silica and phenol/formaldehyde resins – the effect of the support on the liquid phase epoxidation of cyclohexene, Eur. J. Inorg. Chem. 2012 (2012) 251–260, https://doi.org/10.1002/ejic.201101000.
[28] S. Fleischmann, N. Jäckel, M. Zeiger, B. Krüner, I. Grobelsek, P. Formanek, S. Choudhury, D. Weingarth, V. Presser, Enhanced electrochemical energy storage by nanoscopic decoration of endohedral and exohedral carbon with vanadium oxide via atomic layer deposition, Chem. Mater. 28 (2016) 2802–2813, https://doi.org/10.1021/acs.chemmater.6b00738.
[29] W. Wu, K. Ding, J. Liu, T. Drake, P. Stair, E. Weitz, Methanol oxidation to formate on ALD-Prepared VO_x/θ-Al_2O_3 catalysts: a mechanistic study, J. Phys. Chem. C. 121 (2017) 26794–26805, https://doi.org/10.1021/acs.jpcc.7b07498.
[30] S. Boukhalfa, K. Evanoff, G. Yushin, Atomic layer deposition of vanadium oxide on carbon nanotubes for high-power supercapacitor electrodes, Energy Environ. Sci. 5 (2012) 6872, https://doi.org/10.1039/c2ee21110f.
[31] G.-Q. Yang, H. Wang, T. Gong, Y.-H. Song, H. Feng, H.-Q. Ge, H. Ge, Z.-T. Liu, Z.-W. Liu, Understanding the active-site nature of vanadia-based catalysts for oxidative dehydrogenation of ethylbenzene with CO_2 via atomic layer deposited VO_x on γ-Al_2O_3, J. Catal. 380 (2019) 195–203, https://doi.org/10.1016/j.jcat.2019.10.009.
[32] P. Düngen, M. Greiner, K.-H. Böhm, I. Spanos, X. Huang, A.A. Auer, R. Schlögl, S. Heumann, Atomically dispersed vanadium oxides on multiwalled carbon nanotubes via atomic layer deposition: a multiparameter optimization, J. Vac. Sci. Technol. Vac. Surf. Films 36 (2018) 01A126, https://doi.org/10.1116/1.5006783.
[33] J. Keränen, C. Guimon, A. Auroux, E.I. Iiskola, L. Niinistö, Gas-phase synthesis, structure and surface acid–base properties of highly dispersed vanadia/titania/silica catalysts, Phys. Chem. Chem. Phys. 5 (2003) 5333–5342, https://doi.org/10.1039/B307902C.
[34] V.P. Nguyen, J.S. Park, J.M. Yuk, M. Oh, J.-H. Kim, S.-M. Lee, Boosted Zn^{2+} storage performance of hydrated vanadium oxide by defect and heterostructure,

J. Mater. Chem. A 10 (2022) 13428–13438, https://doi.org/10.1039/D2TA03389E.
[35] V.P. Nguyen, I.H. Kim, H.C. Shim, J.S. Park, J.M. Yuk, J.-H. Kim, D. Kim, S.-M. Lee, Porous carbon textile decorated with VC/V_2O_{3-x} hybrid nanoparticles: dual-functional host for flexible Li-S full batteries, Energy Storage Mater. 46 (2022) 542–552, https://doi.org/10.1016/j.ensm.2022.01.027.
[36] M.-G. Willinger, G. Neri, A. Bonavita, G. Micali, E. Rauwel, T. Herntrich, N. Pinna, The controlled deposition of metal oxides onto carbon nanotubes by atomic layer deposition: examples and a case study on the application of V_2O_4 coated nanotubes in gas sensing, Phys. Chem. Chem. Phys. 11 (2009) 3615, https://doi.org/10.1039/b821555c.
[37] M.-G. Willinger, G. Neri, E. Rauwel, A. Bonavita, G. Micali, N. Pinna, Vanadium Oxide Sensing Layer Grown on Carbon Nanotubes by a New Atomic Layer Deposition Process, Nano Lett. 8 (2008) 4201–4204, https://doi.org/10.1021/nl801785b.
[38] X. Wang, Z. Guo, Y. Gao, J. Wang, Atomic layer deposition of vanadium oxide thin films from tetrakis(dimethylamino)vanadium precursor, J. Mater. Res. 32 (2017) 37–44, https://doi.org/10.1557/jmr.2016.303.
[39] J. Peng, J. Brandt, M. Pfeiffer, L.G. Maragno, T. Krekeler, N.T. James, J. Henf, C. Heyn, M. Ritter, M. Eich, A.Yu Petrov, K.P. Furlan, R.H. Blick, R. Zierold, Switchable 3D photonic crystals based on the insulator-to-metal transition in VO_2, ACS Appl. Mater. Interfaces 16 (2024) 67106–67115, https://doi.org/10.1021/acsami.4c13789.
[40] J. Peng, D. Hensel, R. Venugopal, L. Rave, C. Schormann, S. Koch, R.H. Blick, R. Zierold, ALD-Assisted VO_2 for Memristor Application, Adv. Eng. Mater. 27 (2025) 2402614, https://doi.org/10.1002/adem.202402614.
[41] P.A. Premkumar, M. Toeller, I.P. Radu, C. Adelmann, M. Schaekers, J. Meersschaut, T. Conard, S.V. Elshocht, Process study and characterization of VO_2 thin films synthesized by ALD using TEMAV and O_3 precursors, ECS J. Solid State Sci. Technol. 1 (2012) P169–P174, https://doi.org/10.1149/2.009204jss.
[42] F. Mattelaer, K. Geryl, G. Rampelberg, J. Dendooven, C. Detavernier, Amorphous and crystalline vanadium oxides as high-energy and high-power cathodes for three-dimensional thin-film lithium ion batteries, ACS Appl. Mater. Interfaces 9 (2017) 13121–13131, https://doi.org/10.1021/acsami.6b16473.
[43] A.P. Peter, K. Martens, G. Rampelberg, M. Toeller, J.M. Ablett, J. Meersschaut, D. Cuypers, A. Franquet, C. Detavernier, J. Rueff, M. Schaekers, S. Van Elshocht, M. Jurczak, C. Adelmann, I.P. Radu, Metal-insulator transition in ALD VO_2 ultrathin films and nanoparticles: morphological control, Adv. Funct. Mater. 25 (2015) 679–686, https://doi.org/10.1002/adfm.201402687.
[44] K.E. Kapoguzov, S.V. Mutilin, N.I. Lysenko, V.N. Kichay, L.V. Yakovkina, B. V. Voloshin, V.A. Seleznev, Formation of vanadium dioxide nanocrystal arrays via post-growth annealing for stable and energy-efficient switches, Phys. E Low. -Dimens. Syst. Nanostruct. 167 (2025) 116165, https://doi.org/10.1016/j.physe.2024.116165.
[45] P. Guo, M.S. Weimer, J.D. Emery, B.T. Diroll, X. Chen, A.S. Hock, R.P.H. Chang, A.B.F. Martinson, R.D. Schaller, Conformal coating of a phase change material on ordered plasmonic nanorod arrays for broadband all-optical switching, ACS Nano 11 (2017) 693–701, https://doi.org/10.1021/acsnano.6b07042.
[46] Z. Li, F. Wang, X. Wang, Hierarchical branched vanadium oxide Nanorod@Si nanowire architecture for high performance supercapacitors, Small 13 (2017) 1603076, https://doi.org/10.1002/smll.201603076.
[47] I.M. Povey, M. Bardosova, F. Chalvet, M.E. Pemble, H.M. Yates, Atomic layer deposition for the fabrication of 3D photonic crystals structures: growth of Al_2O_3 and VO_2 photonic crystal systems, Surf. Coat. Technol. 201 (2007) 9345–9348, https://doi.org/10.1016/j.surfcoat.2007.04.108.
[48] S. Wang, W. Wei, T. Huang, T. Zhang, Z. Chen, L. Sun, H. Xia, T. Li, X. Chen, X. Chen, W. Lu, N. Dai, Selected-area chemical nanoengineering of vanadium dioxide nanostructures through nonlithographic direct writing, Adv. Mater. Interfaces 5 (2018) 1800974, https://doi.org/10.1002/admi.201800974.
[49] Y. Yang, W. Wei, S. Wang, T. Huang, M. Yuan, R. Zhang, W. Yang, T. Zhang, Y. Sun, Y. Yuan, Z. Yu, X. Chen, N. Dai, Suppression of photoinduced surface oxidation of vanadium dioxide nanostructures by blocking oxygen adsorption, ACS Omega 4 (2019) 17735–17740, https://doi.org/10.1021/acsomega.9b02175.
[50] G.Y. Song, C. Oh, S. Sinha, J. Son, J. Heo, Facile phase control of multivalent vanadium oxide thin films (V_2O_5 and VO_2) by atomic layer deposition and postdeposition annealing, ACS Appl. Mater. Interfaces 9 (2017) 23909–23917, https://doi.org/10.1021/acsami.7b03398.
[51] S. Wang, J. He, P. Sun, Homogeneous Nanostructured VO_2@SiO_2 as an Anti-Reflecting Layer in the Visible/Near Infrared Wavelength, Materials 16 (2023) 6035, https://doi.org/10.3390/ma16176035.
[52] K. Baishya, J. Bacova, B. Al Chimali, J. Capek, J. Michalicka, G. Gautier, B. Le Borgne, T. Rousar, J.M. Macak, Ultrathin ALD Coatings of Zr and V Oxides on Anodic TiO_2 nanotube layers: comparison of the osteoblast cell growth, ACS Appl. Mater. Interfaces 17 (2025) 739–749, https://doi.org/10.1021/acsami.4c19142.
[53] M. Kurttepeli, S. Deng, F. Mattelaer, D.J. Cott, P. Vereecken, J. Dendooven, C. Detavernier, S. Bals, Heterogeneous TiO_2/V_2O_5/carbon nanotube electrodes for lithium-ion batteries, ACS Appl. Mater. Interfaces 9 (2017) 8055–8064, https://doi.org/10.1021/acsami.6b12759.
[54] A. Gervasini, P. Carniti, J. Keranen, L. Niinisto, A. Auroux, Surface characteristics and activity in selective oxidation of -xylene of supported V_2O_5 catalysts prepared by standard impregnation and atomic layer deposition, Catal. Today 96 (2004) 187–194, https://doi.org/10.1016/j.cattod.2004.06.142.
[55] H. Kazerooni, J. Towfighi Darian, Y. Mortazavi, A.A. Khadadadi, R. Asadi, Titania-supported vanadium oxide synthesis by atomic layer deposition and its application for low-temperature oxidative dehydrogenation of propane, Catal. Lett. 150 (2020) 2807–2822, https://doi.org/10.1007/s10562-020-03189-w.
[56] E. Østreng, K.B. Gandrud, Y. Hu, O. Nilsen, H. Fjellvåg, High power nanostructured V_2O_5 thin film cathodes by atomic layer deposition, J. Mater. Chem. A 2 (2014) 15044–15051, https://doi.org/10.1039/C4TA00694A.
[57] C. Liu, N. Kim, G.W. Rubloff, S.B. Lee, High performance asymmetric V_2O_5–SnO_2 nanopore battery by atomic layer deposition, Nanoscale 9 (2017) 11566–11573, https://doi.org/10.1039/C7NR02151H.
[58] C. Liu, E.I. Gillette, X. Chen, A.J. Pearse, A.C. Kozen, M.A. Schroeder, K. E. Gregorczyk, S.B. Lee, G.W. Rubloff, An all-in-one nanopore battery array, Nat. Nanotechnol. 9 (2014) 1031–1039, https://doi.org/10.1038/nnano.2014.247.
[59] E. Pomerantseva, K. Gerasopoulos, X. Chen, G. Rubloff, R. Ghodssi, Electrochemical performance of the nanostructured biotemplated V_2O_5 cathode for lithium-ion batteries, J. Power Sources 206 (2012) 282–287, https://doi.org/10.1016/j.jpowsour.2012.01.127.
[60] M. Xie, X. Sun, H. Sun, T. Porcelli, S.M. George, Y. Zhou, J. Lian, Stabilizing an amorphous V_2O_5/carbon nanotube paper electrode with conformal TiO_2 coating by atomic layer deposition for lithium ion batteries, J. Mater. Chem. A 4 (2015) 537–544, https://doi.org/10.1039/C5TA01949D.
[61] F. Ye, D. Lu, X. Gui, T. Wang, X. Zhuang, W. Luo, Y. Huang, Atomic layer deposition of core-shell structured V_2O_5@CNT sponge as cathode for potassium ion batteries, J. Mater. 5 (2019) 344–349, https://doi.org/10.1016/j.jmat.2018.05.009.
[62] J.W. Elam, G. Xiong, C.Y. Han, H.H. Wang, J.P. Birrell, U. Welp, J.N. Hryn, M. J. Pellin, T.F. Baumann, J.F. Poco, J.H. Satcher, Atomic layer deposition for the conformal coating of nanoporous materials, J. Nanomater 2006 (2006) 064501, https://doi.org/10.1155/JNM/2006/64501.
[63] H. Groult, E. Balnois, A. Mantoux, K. Le Van, D. Lincot, Two-dimensional recrystallisation processes of nanometric vanadium oxide thin films grown by atomic layer chemical vapor deposition (ALCVD) evidenced by AFM, Appl. Surf. Sci. 252 (2006) 5917–5925, https://doi.org/10.1016/j.apsusc.2005.08.014.
[64] I.E. Rauda, V. Augustyn, L.C. Saldarriaga-Lopez, X. Chen, L.T. Schelhas, G. W. Rubloff, B. Dunn, S.H. Tolbert, Nanostructured pseudocapacitors based on atomic layer deposition of V_2O_5 onto Conductive Nanocrystal-based Mesoporous ITO Scaffolds, Adv. Funct. Mater. 24 (2014) 6717–6728, https://doi.org/10.1002/adfm.201401284.
[65] S. Chung, S. Bong, J. Lee, Atomic layer deposition of vanadium pentoxide on carbon electrode for enhanced capacitance performance in capacitive deionization, Appl. Chem. Eng. 33 (2022) 315–321, https://doi.org/10.14478/ACE.2022.1020.
[66] X. Chen, E. Pomerantseva, P. Banerjee, K. Gregorczyk, R. Ghodssi, G. Rubloff, Ozone-based atomic layer deposition of crystalline V_2O_5 films for high performance electrochemical energy storage, Chem. Mater. 24 (2012) 1255–1261, https://doi.org/10.1021/cm202901z.
[67] J.S. Daubert, N.P. Lewis, H.N. Gotsch, J.Z. Mundy, D.N. Monroe, E.C. Dickey, M. D. Losego, G.N. Parsons, Effect of meso- and micro-porosity in carbon electrodes on atomic layer deposition of pseudocapacitive V_2O_5 for high performance supercapacitors, Chem. Mater. 27 (2015) 6524–6534, https://doi.org/10.1021/acs.chemmater.5b01602.
[68] J.S. Daubert, R. Wang, J.S. Ovental, H.F. Barton, R. Rajagopalan, V. Augustyn, G. N. Parsons, Intrinsic limitations of atomic layer deposition for pseudocapacitive metal oxides in porous electrochemical capacitor electrodes, J. Mater. Chem. A 5 (2017) 13086–13097, https://doi.org/10.1039/C7TA02719B.
[69] S. Fleischmann, D. Leistenschneider, V. Lemkova, B. Krüner, M. Zeiger, L. Borchardt, V. Presser, Tailored mesoporous carbon/vanadium pentoxide hybrid electrodes for high power pseudocapacitive lithium and sodium intercalation, Chem. Mater. 29 (2017) 8653–8662, https://doi.org/10.1021/acs.chemmater.7b02533.
[70] X. Chen, H. Zhu, Y.-C. Chen, Y. Shang, A. Cao, L. Hu, G.W. Rubloff, MWCNT/V_2O_5 core/shell sponge for high areal capacity and power density Li-Ion Cathodes, ACS Nano 6 (2012) 7948–7955, https://doi.org/10.1021/nn302417x.
[71] R. Carter, L. Oakes, N. Muralidharan, A.P. Cohn, A. Douglas, C.L. Pint, Polysulfide anchoring mechanism revealed by atomic layer deposition of V_2O_5 and sulfur-filled carbon nanotubes for lithium–sulfur batteries, ACS Appl. Mater. Interfaces 9 (2017) 7185–7192, https://doi.org/10.1021/acsami.6b16155.
[72] S. Santangelo, G. Messina, G. Faggio, M.-G. Willinger, N. Pinna, A. Donato, A. Arena, N. Donato, G. Neri, Micro-Raman investigation of vanadium-oxide coated tubular carbon nanofibers for gas-sensing applications, Diam. Relat. Mater. 19 (2010) 590–594, https://doi.org/10.1016/j.diamond.2009.11.014.
[73] J. Keränen, C. Guimon, E. Iiskola, A. Auroux, L. Niinisto, Surface-controlled gas-phase deposition and characterization of highly dispersed vanadia on silica, J. Phys. Chem. B 107 (2003) 10773–10784, https://doi.org/10.1021/jp030385i.
[74] S.-M. Lee, Y.-J. Park, D.V. Lam, J.-H. Kim, K. Lee, Effects of annealing on electrochemical performance in graphene/V_2O_5 supercapacitor, Appl. Surf. Sci. 512 (2020) 145626, https://doi.org/10.1016/j.apsusc.2020.145626.
[75] C. Hedrich, D. Deduytsche, R.R. Petit, T. Krekeler, J. Peng, M. Ritter, J. Dendooven, C. Detavernier, R.H. Blick, R. Zierold, Tuning the crystallization temperature of titanium dioxide thin films by incorporating silicon dioxide via supercycle atomic layer deposition, Surf. Interfaces 57 (2025) 105696, https://doi.org/10.1016/j.surfin.2024.105696.
[76] J.P. Wooding, S.A. Gregory, A. Atassi, G. Freychet, K. Kalaitzidou, M.D. Losego, Transformation kinetics for low temperature post-deposition crystallization of TiO_2 thin films prepared via atomic layer deposition (ALD) from tetrakis (dimethylamino)titanium(IV) (TDMAT) and water, ALDJ 1 (2023) 1–18, https://doi.org/10.3897/aldj.1.101276.

[77] J.P. Wooding, K. Kalaitzidou, M.D. Losego, Crystalline as-deposited TiO 2 anatase thin films grown from TDMAT and water using thermal atomic layer deposition with in situ layer-by-layer air annealing, . Layer. Depos. 2 (2024) 1–18, https://doi.org/10.3897/aldj.2.117753.
[78] Z. Yu, B. Saini, Y. Liu, F. Huang, A. Mehta, J.D. Baniecki, H.-S.P. Wong, W. Tsai, P.C. McIntyre, Nanocrystallite seeding of metastable ferroelectric phase formation in atomic layer-deposited hafnia–zirconia alloys, ACS Appl. Mater. Interfaces 14 (2022) 53057–53064, https://doi.org/10.1021/acsami.2c15047.
[82] E. Pomerantseva, K. Gerasopoulos, X. Chen, G. Rubloff, R. Ghodssi, Electrochemical performance of the nanostructured biotemplated V_2O_5 cathode for lithium-ion batteries, J. Power Sources 206 (2012) 282–287, https://doi.org/10.1016/j.jpowsour.2012.01.127.
[83] C. Hedrich, N.T. James, L.G. Maragno, V. De Lima, S.Y.G. González, R.H. Blick, R. Zierold, K.P. Furlan, Enhanced photocatalytic properties and photoinduced crystallization of TiO_2 –Fe_2O_3 inverse opals fabricated by atomic layer deposition, ACS Appl. Mater. Interfaces 16 (2024) 46964–46974, https://doi.org/10.1021/acsami.4c10831.
[84] I. Bretos, R. Jiménez, J. Ricote, M.L. Calzada, Low-temperature crystallization of solution-derived metal oxide thin films assisted by chemical processes, Chem. Soc. Rev. 47 (2018) 291–308, https://doi.org/10.1039/C6CS00917D.
[85] G. Krylova, C. Na, Photoinduced crystallization and activation of amorphous titanium dioxide, J. Phys. Chem. C. 119 (2015) 12400–12407, https://doi.org/10.1021/acs.jpcc.5b02048.
[86] C. Hedrich, D. Deduytsche, R.R. Petit, T. Krekeler, J. Peng, M. Ritter, J. Dendooven, C. Detavernier, R.H. Blick, R. Zierold, Tuning the crystallization temperature of titanium dioxide thin films by incorporating silicon dioxide via supercycle atomic layer deposition, Surf. Interfaces 57 (2025) 105696, https://doi.org/10.1016/j.surfin.2024.105696.
[87] M. Weber, A. Julbe, A. Ayral, P. Miele, M. Bechelany, Atomic layer deposition for membranes: basics, challenges, and opportunities, Chem. Mater. 30 (2018) 7368–7390, https://doi.org/10.1021/acs.chemmater.8b02687.
[88] J. Peng, R. Zierold, Atomic layer deposition of materials, in: Encycl. Condens. Matter Phys, Elsevier, 2024, pp. 716–728, https://doi.org/10.1016/B978-0-323-90800-9.00206-7.
[89] B. Chen, G. Kim, H.J. Cho, H. Ohta, Room temperature insulator-to-metal transition of VO_2 /TiO_2 epitaxial bilayer films grown on M-plane Sapphire Substrates, Adv. Electron. Mater. 8 (2022) 2100687, https://doi.org/10.1002/aelm.202100687.
[90] B. Chen, C. Yang, B. Feng, Y. Ikuhara, H. Ohta, Suppression of Strain Relaxation in VO_2/TiO_2 Multilayered Films, ACS Appl. Electron. Mater. 5 (2023) 2433–2438, https://doi.org/10.1021/acsaelm.3c00246.
[91] L. Chen, Y. Cui, H. Luo, Y. Gao, Tuning thE Metal–insulator Transition in TiO_2/VO_2 superlattices by modifying the layer thickness or inducing defects, J. Phys. Chem. C. 126 (2022) 6016–6027, https://doi.org/10.1021/acs.jpcc.2c00091.
[92] X. Li, R.E. Schaak, Size- and interface-modulated metal–insulator transition in solution-synthesized nanoscale VO_2 -TiO_2 -VO_2 heterostructures, Angew. Chem. Int. Ed. 56 (2017) 15550–15554, https://doi.org/10.1002/anie.201706599.
[93] Q. Lu, C. Sohn, G. Hu, X. Gao, M.F. Chisholm, I. Kylänpää, J.T. Krogel, P.R. C. Kent, O. Heinonen, P. Ganesh, H.N. Lee, Metal–insulator transition tuned by oxygen vacancy migration across TiO_2/VO_2 interface, Sci. Rep. 10 (2020) 18554, https://doi.org/10.1038/s41598-020-75695-1.
[94] C.N. Mihailescu, E. Symeou, E. Svoukis, R.F. Negrea, C. Ghica, V. Teodorescu, L. C. Tanase, C. Negrila, J. Giapintzakis, Ambiguous role of growth-induced defects on the semiconductor-to-metal characteristics in epitaxial VO_2/TiO_2 thin films, ACS Appl. Mater. Interfaces 10 (2018) 14132–14144, https://doi.org/10.1021/acsami.8b01436.
[95] M. Soltani, M. Chaker, E. Haddad, R.V. Kruzelecky, J. Margot, Effects of Ti–W codoping on the optical and electrical switching of vanadium dioxide thin films grown by a reactive pulsed laser deposition, Appl. Phys. Lett. 85 (2004) 1958–1960, https://doi.org/10.1063/1.1788883.
[96] Y. Wu, L. Fan, Q. Liu, S. Chen, W. Huang, F. Chen, G. Liao, C. Zou, Z. Wu, Decoupling the lattice distortion and charge doping effects on the phase transition behavior of VO_2 by Titanium (Ti^{4+}) Doping, Sci. Rep. 5 (2015) 9328, https://doi.org/10.1038/srep09328.
[97] Y. Zheng, Z. Chen, H. Lu, Y. Cheng, X. Chen, Y. He, Z. Zhang, The formation of TiO_2/VO_2 multilayer structure via directional cationic diffusion, Nanoscale 13 (2021) 7783–7791, https://doi.org/10.1039/D1NR00290B.
[98] M. Yang, Y. Yang, Bin Hong, L. Wang, K. Hu, Y. Dong, H. Xu, H. Huang, J. Zhao, H. Chen, L. Song, H. Ju, J. Zhu, J. Bao, X. Li, Y. Gu, T. Yang, X. Gao, Z. Luo, C. Gao, Suppression of Structural Phase Transition in VO_2 by Epitaxial Strain in Vicinity of Metal-insulator Transition, Sci. Rep. 6 (2016) 23119, https://doi.org/10.1038/srep23119.
[99] C. Hedrich, A.R. Burson, S. González-García, V. Vega, V.M. Prida, A. Santos, R. H. Blick, R. Zierold, Enhancing the photocatalytic activity by tailoring an anodic aluminum oxide photonic crystal to the semiconductor catalyst: at the example of iron oxide, Adv. Mater. Interfaces 10 (2023) 2300615, https://doi.org/10.1002/admi.202300615.
[100] M. Leskelä, E. Salmi, M. Ritala, Atomic layer deposited protective layers, Mater. Sci. Forum 879 (2017) 1086–1092, https://doi.org/10.4028/www.scientific.net/MSF.879.1086.
[101] J. Lu, J.W. Elam, P.C. Stair, Synthesis and stabilization of supported metal catalysts by atomic layer deposition, Acc. Chem. Res. 46 (2013) 1806–1815, https://doi.org/10.1021/ar300229c.
[102] W.J. Lee, S. Bera, H. Woo, H.G. Kim, J.H. Baek, W. Hong, J.Y. Park, S.J. Oh, S. H. Kwon, Situ engineering of a metal oxide protective layer into Pt/carbon fuel-cell catalysts by atomic layer deposition, Chem. Mater. 34 (2022) 5949–5959, https://doi.org/10.1021/acs.chemmater.2c00928.
[103] J.A. Singh, N. Yang, S.F. Bent, Nanoengineering heterogeneous catalysts by atomic layer deposition, Annu. Rev. Chem. Biomol. Eng. 8 (2017) 41–62, https://doi.org/10.1146/annurev-chembioeng-060816-101547.
[104] B.J. Oneill, D.H.K. Jackson, J. Lee, C. Canlas, P.C. Stair, C.L. Marshall, J.W. Elam, T.F. Kuech, J.A. Dumesic, G.W. Huber, Catalyst design with atomic layer deposition, ACS Catal. 5 (2015) 1804–1825, https://doi.org/10.1021/cs501862h.